Implicit Solution of Three-Dimensional Internal Turbulent Flows

V. Michelassi*
Institute for Computational Mechanics in Propulsion
NASA Lewis Research Center
Cleveland, Ohio

M.-S. Liou and L.A. Povinelli
National Aeronautics and Space Administration
Lewis Research Center
Cleveland, Ohio

and

F. Martelli
University of Florence
Florence, Italy

ABSTRACT

The scalar form of the approximate factorization method was used to develop a new code for the solution of three-dimensional internal laminar and turbulent compressible flows. The Navier-Stokes equations in their Reynolds-averaged form were iterated in time until a steady solution was reached. Evidence was given to the implicit and explicit artificial damping schemes that proved to be particularly efficient in speeding up convergence and enhancing the algorithm robustness. A conservative treatment of these terms at the domain boundaries was proposed in order to avoid undesired mass and/or momentum artificial fluxes. Turbulence effects were accounted for by the zero-equation Baldwin-Lomax turbulence model and the q-ω two-equation model. For the first, an investigation on the model behavior in case of multiple boundaries was performed. The flow in a developing S-duct was then solved in laminar regime at a Reynolds number (Re) of 790 and in a turbulent regime at Re=40,000 by using the Baldwin-Lomax model. The Stanitz elbow was then solved by using an inviscid version of the same code at M_{inlet}=0.4. Grid dependence and convergence rate were investigated showing that for this solver the implicit damping scheme may play a critical role for convergence characteristics. The same flow at Re=$2.5 \cdot 10^6$ was solved with the Baldwin-Lomax and the q-ω models. Both approaches showed satisfactory agreement with experiments, although the q-ω model was slightly more accurate.

INTRODUCTION

With the advent of more and more powerful supercomputers, the numerical solution of three-dimensional turbulent flows became possible (ref. 1). Although it is well known that lower order turbulence closures fail to reproduce secondary motions of Prandtl's second kind (turbulence driven), they normally succeed in predicting secondary flows of the first kind (pressure driven). Therefore, for many complex configurations it has been possible to obtain fairly accurate results with zero- and two-equation turbulence models (ref. 2) with a reasonable prediction of pressure driven secondary flows.

For three-dimensional blade-passage flows, a correct prediction of the wake behavior was obtained by Yokota (ref. 3) by means of the standard high-Reynolds-number form of the k-ϵ two-equation model with the wall function approach. However, the zero-equation model implemented in reference 3 did not give a satisfactory depiction of the flow in the wake region. For the prediction of blade pressure distribution, the

*On leave from the University of Florence, Italy.

Work funded by Space Act Agreement C99066G.

Baldwin-Lomax (ref. 4) zero-equation turbulence model was found to give accurate results in several flow configurations (ref. 5) despite the low convergence rate. For incompressible internal flows with no separation, good results were obtained by Towne (ref. 6) with a zero-equation turbulence model and a parabolized Navier-Stokes solver. Still, for practical flow configurations, quite long computing times are necessary mainly because of the large number of points usually required for a detailed description of the flow field. Moreover, the nonlinearities associated with nearly all turbulence models can play a significant role in slowing down the convergence rate to the steady state solution. This behavior occurs in both the implicit and explicit flow solvers and is intrinsic to the turbulence models, zero or two-equation.

In two dimensions, a wide variety of flow conditions have been accurately solved by means of low-Reynolds-number forms of the k-ϵ model in which the effect of laminar viscosity is explicitly accounted for (refs. 7 to 9). In nearly all of the flow conditions investigated, these forms proved to be more accurate than the standard high-Re formulation, provided that a sufficient number of grid points were located inside the viscous and buffer layers; in fact, secondary motions and losses are mainly driven by what happens close to walls so that a correct description of this flow region is crucial for an accurate simulation of the flow pattern. Rodi (ref. 9) found that the low Reynolds number forms of the k-ϵ model could predict secondary flows that are normally lost with the high Reynolds number form. Unfortunately, the first author (ref. 7) found that some of these forms were extremely stiff from a numerical point of view. The stiffness was mainly caused by the low-Reynolds-number effect terms in which exponential functions are introduced to model the wall effects.

From this standpoint, it appeared worthwhile to investigate some features of turbulence models for internal turbulent flows by using an implicit algorithm. Since complex flow patterns, such as separation and dominant viscous effects, are expected in internal flows, the implicit approach was selected to increase the robustness and convergence rate of the numerical procedure when zero and two-equation turbulence models are used.

DESCRIPTION OF THE ALGORITHM

Navier-Stokes Equations

The Boussinesq hypothesis allows the turbulent shear stresses to be related to the mean strains via the so-called eddy viscosity so that, under this assumption, the three-dimensional Reynolds-averaged compressible Navier-Stokes (N-S) equations can be written in divergence form and, subsequently, be transformed from the Cartesian coordinate system (x,y,z) to the generalized curvilinear coordinate system (ξ,η,ζ). The resulting set of equations can be written in vector form as follows:

$$\frac{\partial \overline{Q}}{\partial t} + \frac{\partial \overline{E}}{\partial \xi} + \frac{\partial \overline{F}}{\partial \eta} + \frac{\partial \overline{G}}{\partial \zeta} = \frac{\partial \overline{E}_v}{\partial \xi} + \frac{\partial \overline{F}_v}{\partial \eta} + \frac{\partial \overline{G}_v}{\partial \zeta}$$

where $\overline{Q}$ is the vector of unknowns; $\overline{E}$, $\overline{F}$, and $\overline{G}$ are the flux vectors of the convective terms; $\overline{E}_v$, $\overline{F}_v$, and $\overline{G}_v$ are the flux vectors of the diffusive terms, the complete definition of which can be found in reference 19.

In the set of equations, ρ is the fluid density, p is the static pressure, e is the total energy per unit volume, a is the sound speed, and (U,V,W) are the Cartesian components of the velocity vector. According to the Boussinesq assumption, the diffusion coefficients for momentum and energy are defined as follows:

$$\mu_{eff} = \mu_l + \mu_t \quad \text{and} \quad \mu_h = \frac{\mu_l}{Pr_l} + \frac{\mu_t}{Pr_t}$$

in which μ_l is the laminar viscosity, which was considered to be independent of the static temperature, and μ_t is the turbulent viscosity obtained from the turbulence model. In this set of calculations the turbulent

Prandtl number Pr_t was set equal to 0.90 and the laminar Prandtl number Pr_l was 0.72.

Discretization

The flux vectors are discretized by using centered finite differences. The metrics are usually obtained from a chain rule expansion of x_ξ, x_η, x_ζ, y_ξ, y_η, y_ζ, z_ξ, z_η, and z_ζ. When the centered discretization is used for the metrics, it can be shown that in three dimensions the metric invariants are not satisfied (ref. 10). This may result in a large discretization error. However, it is possible to satisfy the invariants by a simple averaging technique that gives metrics that are similar to those computed by a finite volume method. For example, ξ_x is computed as follows

$$\xi_x = J\left(\chi_\zeta\left(\frac{\partial y}{\partial \eta}\right) \chi_\eta\left(\frac{\partial z}{\partial \zeta}\right) - \chi_\eta\left(\frac{\partial y}{\partial \zeta}\right) \chi_\zeta\left(\frac{\partial z}{\partial \eta}\right)\right)$$

in which J is the Jacobian of the coordinate transformation and χ is a central average operator. This averaging process was found to ensure better mass conservation properties in the present calculations expecially for highly stretched grids.

Approximate Factorization; Scalar Form

The approximate factorization method first proposed by Beam and Warming (ref. 11) splits an n-dimensional operator into the product of n one-dimensional operators. This technique provides a strong link between the equations insofar as they are solved fully coupled. The main drawback of this method lies in the necessity of a time-consuming block tridiagonal or pentadiagonal matrix inversion. This problem becomes more evident in three dimensions where the coupled solution yields a 5×5 block tridiagonal matrix. In order to make this algorithm more efficient and still maintain its strong implicit nature Pulliam (refs. 10 and 12) proposed a scalar form of the approximate factorization. The form of the standard algorithm in three dimensions can be written as follows:

$$[\, I+\Theta\Delta t\left(\delta_\xi A - \delta_\xi^2 A_v\right)]*[\, I+\Theta\Delta t\left(\delta_\eta B - \delta_\eta^2 B_v\right)]*[\, I+\Theta\Delta t\left(\delta_\zeta C - \delta_\zeta^2 C_v\right)]*\Delta Q = RHS \tag{1}$$

in which I is the identity matrix; θ is a parameter that allows the explicit-implicit nature of the space operator to be weighted (in the present calculations, since the steady state solution was sought, θ=1 was used which gave first-order accuracy in time); δ is a centered difference operator; Δt is the time step; $\Delta Q = Q^{n+1} - Q^n$; $Q = J\,\overline{Q}$; A, B, and C are the convective Jacobians; A_v, B_v, and C_v are the diffusive Jacobians in the three directions ξ, η, and ζ; and RHS represents the convective and diffusive fluxes and is defined as

$$RHS = \Delta t\left(-\frac{\partial \overline{E}}{\partial \xi} - \frac{\partial \overline{F}}{\partial \eta} - \frac{\partial \overline{G}}{\partial \zeta} + \frac{\partial \overline{E}_v}{\partial \xi} + \frac{\partial \overline{F}_v}{\partial \eta} + \frac{\partial \overline{G}_v}{\partial \zeta}\right)$$

The Jacobian matrices A, B, C, A_v, B_v, and C_v, which can be found in Pulliam (ref. 10), are full and require a general inversion process. Pulliam and Chaussee (ref. 12) proposed a more efficient procedure by making some simplifications. First, the hyperbolic property of the convective Jacobians allows the diagonalization as

$$A = T_\xi \Lambda_\xi T_\xi^{-1} \;;\quad B = T_\eta \Lambda_\eta T_\eta^{-1} \;;\quad C = T_\zeta \Lambda_\zeta T_\zeta^{-1} \tag{2}$$

in which T are the eigenvector matrices, defined in reference 12. The eigenvalues of the Jacobians in three dimensions, Λ, are given by

$$\Lambda_\xi = D\,[U,\ U,\ U,\ U+a\sqrt{\xi_x^2+\xi_y^2+\xi_z^2},\ U-a\sqrt{\xi_x^2+\xi_y^2+\xi_z^2}]$$
$$\Lambda_\eta = D\,[V,\ V,\ V,\ V+a\sqrt{\eta_x^2+\eta_y^2+\eta_z^2},\ V-a\sqrt{\eta_x^2+\eta_y^2+\eta_z^2}] \qquad (3)$$
$$\Lambda_\zeta = D\,[W,\ W,\ W,\ W+a\sqrt{\zeta_x^2+\zeta_y^2+\zeta_z^2},\ W-a\sqrt{\zeta_x^2+\zeta_y^2+\zeta_z^2}]$$

where U, V, and W are the unscaled contravariant velocities and D stands for main diagonal only. It is now possible to introduce equations (2) into equation (1) with eigenvalues defined in equation (3). Doing so, it is impossible to diagonalize both the convective and diffusive Jacobians since they have a totally different set of eigenvectors. Neglecting the diffusive Jacobians and assuming the eigenmatrix to be locally constant, equation (1) can be rewritten as

$$T_\xi * [I+\Theta\Delta t(\delta_\xi \Lambda_\xi)] * N * [I+\Theta\Delta t(\delta_\eta \Lambda_\eta)] * P * [I+\Theta\Delta t(\delta_\zeta \Lambda_\zeta)] * T_\zeta^{-1} * \Delta Q = RHS \qquad (4)$$

in which the two matrices, $N=T_\xi^{-1}\,T_\eta$ and $P=T_\eta^{-1}\,T_\zeta$ have the nice property of being solution independent so that they can be computed only once (ref. 12). Obviously, equation (4) is only an approximation of the full form but it requires only a scalar tridiagonal or pentadiagonal matrix inversion since the Λ matrices are diagonal; this implies a reduction of nearly 50% of the operations required by the standard algorithm. We note that, even though the interior domain is solved implicitly, the boundary conditions are imposed in a fully explicit manner. This was done by setting $\Delta Q=0$ at the domain boundaries during the implicit sweeps.

Since the steady state solution is sought, the following local time-stepping formula, based on the approximate constant CFL condition is introduced, in which the contribution of the diffusive terms is accounted for

$$\Delta t_\xi = |U| + a\sqrt{\xi_x^2+\xi_y^2+\xi_z^2} + \mu_{eff}\,Re^{-1}\,(\xi_x^2+\xi_y^2+\xi_z^2)$$
$$\Delta t_\eta = |V| + a\sqrt{\eta_x^2+\eta_y^2+\eta_z^2} + \mu_{eff}\,Re^{-1}\,(\eta_x^2+\eta_y^2+\eta_z^2)$$
$$\Delta t_\zeta = |W| + a\sqrt{\zeta_x^2+\zeta_y^2+\zeta_z^2} + \mu_{eff}\,Re^{-1}\,(\zeta_x^2+\zeta_y^2+\zeta_z^2)$$
$$\Delta t = \frac{CFL}{\Delta t_\xi + \Delta t_\eta + \Delta t_\zeta}$$

Implicit Treatment of Diffusive Terms

For inviscid solutions, the only assumption done to derive the algorithm is that the differentiation of the eigenmatrices is neglected in equation (4). In addition, when solving the N-S equations, the Jacobians of the diffusive terms are normally assumed to be negligible. This does not cause any stability or convergence problems for external flows where the diffusion dominated region is small and restricted to a limited part of the computational domain. But this simplification may cause troubles for internal flows where the diffusion dominated region can be large. According to this, for internal flows it is convenient to introduce an approximation of the eigenvalues of the diffusive terms jacobian and put it into equation (4). Two forms of this approximation have been considered.

- Pulliam's approximation.

Pulliam (ref. 10) proposes an approximate form of the diffusive Jacobian eigenvalues that was obtained by intense numerical testing. This form is

$$\Lambda^v_\xi = (\rho\ \mu_{eff}\ Re^{-1}\ (\xi_x{}^2+\xi_y{}^2+\xi_z{}^2)\ J^{-1}) \cdot D\ [1,1,1,1,1]$$
$$\Lambda^v_\eta = (\rho\ \mu_{eff}\ Re^{-1}\ (\eta_x{}^2+\eta_y{}^2+\eta_z{}^2)\ J^{-1}) \cdot D\ [1,1,1,1,1] \qquad (5)$$
$$\Lambda^v_\zeta = (\rho\ \mu_{eff}\ Re^{-1}\ (\zeta_x{}^2+\zeta_y{}^2+\zeta_z{}^2)\ J^{-1}) \cdot D\ [1,1,1,1,1]$$

In the present set of calculations it was found convenient not to weight the eigenvalues with the Jacobian of the coordinate transformation J^{-1}. These expressions are included on the implicit side of equation (4): for instance, the ξ direction implicit operator reads

$$[\ I + \Theta\ \Delta t\ (\delta_\xi\ \Lambda_\xi - \delta^2_\xi \Lambda^v_\xi)\ ]$$

• Present approximation.
The exact form of the diffusive terms Jacobian can be computed from the related flux vectors. For the three sweeps the main diagonal of such matrix may be conveniently approximated as

$$\Lambda_\xi{}^v = D\ [0,\alpha_\xi,\alpha_\xi,\alpha_\xi,\gamma\ Pr^{-1}\alpha_\xi]$$
$$\Lambda_\eta{}^v = D\ [0,\alpha_\eta,\alpha_\eta,\alpha_\eta,\gamma\ Pr^{-1}\alpha_\eta] \qquad (6)$$
$$\Lambda_\zeta{}^v = D\ [0,\alpha_\zeta,\alpha_\zeta,\alpha_\zeta,\gamma\ Pr^{-1}\alpha_\zeta]$$

in which

$$\alpha_\xi = \mu_{eff}\ Re^{-1}\ J^{-1}\ (\xi_x{}^2+\xi_y{}^2+\xi_z{}^2)\ \frac{\partial(\rho^{-1}J)}{\partial\xi}$$

$$\alpha_\eta = \mu_{eff}\ Re^{-1}\ J^{-1}\ (\eta_x{}^2+\eta_y{}^2+\eta_z{}^2)\ \frac{\partial(\rho^{-1}J)}{\partial\eta}$$

$$\alpha_\zeta = \mu_{eff}\ Re^{-1}\ J^{-1}\ (\zeta_x{}^2+\zeta_y{}^2+\zeta_z{}^2)\ \frac{\partial(\rho^{-1}J)}{\partial\zeta}$$

Regarding the extra-diagonal terms as negligible, the previous diagonal matrices are a good approximation of the diffusive terms Jacobians and can be put into the implicit side of equation (4): for instance, the ξ direction implicit operator reads

$$[\ I + \Theta\ \Delta t\ (\delta_\xi\ \Lambda_\xi - \delta_\xi \Lambda^v_\xi)\ ]$$

in which the diffusive terms contribution is approximated as a first order derivative. It is possible to prove that the first approximation increases the main diagonal dominance by summing to it an extra term, whereas in the second approximation an artificial term is subtracted from the off-diagonal components while leaving the main diagonal unchanged. A comparison of the two approaches, equations (5) and (6), was performed on a simple straight channel geometry at $Re \simeq 1000$ and $M_{inlet}=0.3$ in a laminar flow regime. For this very simple flow configuration there were no differences in convergence rate between the two approaches, and it was also possible to drop the diffusive terms on the implicit side of equation (4) without altering convergence. Differences started to appear at $Re=50$ because of the highly diffusive nature

of the flow. Figure 1(a) shows the best convergence history of the algorithm without any implicit treatment of the diffusive terms that were obtained at CFL=5. (The lower curve refers to the averaged residuals, and the upper curve refers to the maximum.) Figures 1(b) and 1(c) refer to equations (5) and (6). There are no appreciable differences between the two convergence rates obtained at CFL=10 since both curves show nearly the same slope. The same result could be obtained if the Baldwin-Lomax turbulence model was used. At least for this class of flows the approximate implicit treatment of diffusive terms given by equation (6) did not prove to be more efficient than equation (5). Further testing is necessary in order to verify this result at higher Mach numbers when differences in the convergence between equations (5) and (6) may appear since the density derivatives do not tend to vanish for compressible flows rather than for incompressible flows.

(*a*) - *no. diff. terms* (*b*) - *approximation* (5) (*c*) - *approximation* (6)

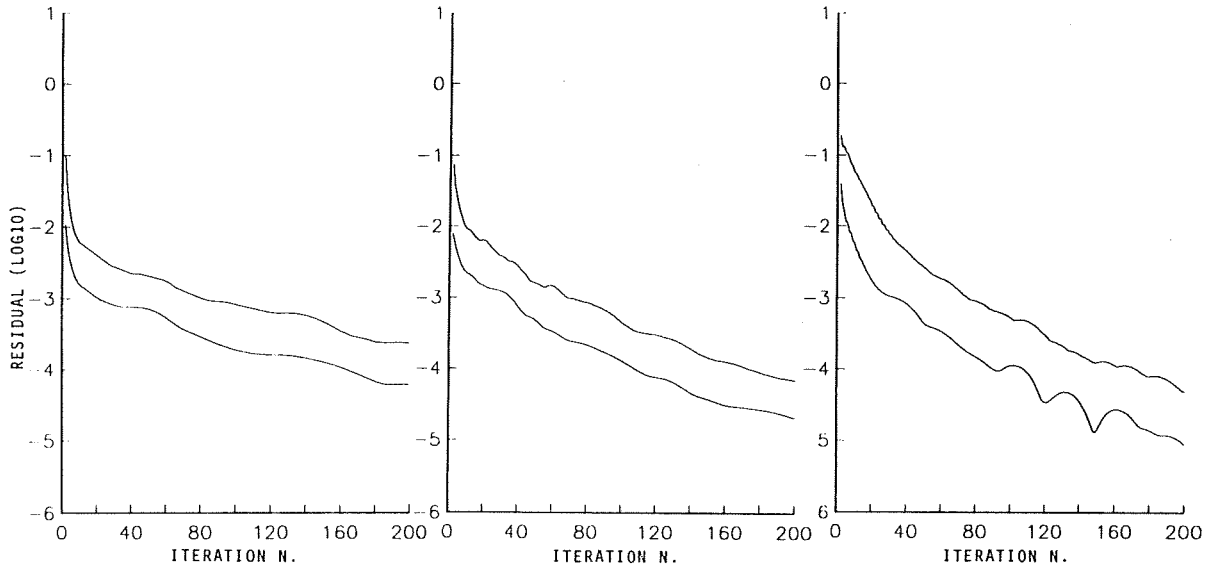

Figure 1. Convergence tests for implicit treatment of diffusive terms.

Added Explicit and Implicit Damping

When using centered finite differences, it is necessary to introduce an artificial damping scheme in order to prevent odd-even velocity-pressure decoupling that occurs whenever the local Peclet number exceeds 2 in large-gradient regions. Moreover, the three-dimensional approximate factorization method can be proved to be unconditionally unstable since, when performing a linear stability analysis, one of the amplification factors is found to be slightly larger than one. This weak instability can be easily overcome by using an artificial damping scheme. From the two-dimensional version of the approximate factorization, it is also known that fourth order artificial damping is necessary to damp the numerical modes associated with the highest frequencies. Following the basic guideline given by Jameson et al. (ref. 13) and Pulliam (ref. 14), a blended implicit-explicit second plus fourth order nonlinear damping scheme was introduced in the present solver.

- Explicit 2^{nd} and 4^{th} order damping.

In the original formulation, the artificial damping is simply equally scaled according to the local Δt in the three space directions. This could be done mainly because the damping scheme has been first applied to inviscid flows. For viscous flow calculations, Pulliam (ref. 10) found it convenient to scale the damping terms according to the directional spectral radius σ. The scheme for the ξ direction sweep yields

C-5

$$D_\xi^{(2)}+D_\xi^{(4)} = \delta_\xi\left(\left((\sigma J^{-1})_{i+1,j,k}+(\sigma J^{-1})_{i,j,k}\right)\left(\omega_{i,j,k}^{(2)}\delta_\xi\,(Q_{i,j,k}) - \omega_{i,j,k}^{(4)}\delta_\xi(Q_{i,j,k})\right)\right) \tag{7}$$

The complete definitions of $\omega^{(2)}$ and $\omega^{(4)}$ are given following Pulliam

$$\Upsilon_{i,j,k} = \frac{\left|p_{i+1,j,k} - 2p_{i,j,k} + p_{i-1,j,k}\right|}{\left|p_{i+1,j,k} + 2p_{i,j,k} + p_{i-1,j,k}\right|}$$

$$\omega_{i,j,k}^{(2)} = \Omega^{(2)}\,\Delta t\; max(\Upsilon_{i-1,j,k},\, \Upsilon_{i,j,k},\, \Upsilon_{i+1,j,k})$$

$$\omega_{i,j,k}^{(4)} = max(0.,\, \Omega^{(4)}\,\Delta t - \omega_{i,j,k}^{(2)}) \tag{8}$$

and the unscaled spectral radius is defined as

$$\sigma_{i,j,k} = |U| + a\sqrt{\xi_x^2 + \xi_y^2 + \xi_z^2}$$

Since the present set of calculations has been performed for shock-free flow fields, the shock sensor term defined in equation (8) was switched off by always taking $\Upsilon_{i,j,k}$. Nevertheless, this modification does not really affect the damping scheme since the second order term is active only in presence of shocks. Actually, this scheme gives only fourth order damping in smooth shock-free flow fields so that in most of the calculations $\Omega^{(2)}$ was set equal to zero whereas the fourth order weight, $\Omega^{(4)}$, ranges from 1/16 to 1/12.8.

Equation (7) is then added to the RHS of equation (4),

$$RHS = RHS + \Delta t\,(D_\xi^{(2)} + D_\xi^{(4)} + D_\eta^{(2)} + D_\eta^{(4)} + D_\zeta^{(2)} + D_\zeta^{(4)})$$

• Implicit 2^{nd} or 4^{th} order damping.

To enhance the algorithm stability and convergence rate, it is helpful to include the artificial damping terms on the implicit side. For both the 2^{nd} and the 4^{th} order damping, the implicit treatment augments the diagonal dominance of the scalar system with a beneficial effect on the convergence rate. As it was pointed out by Pulliam (ref. 10), there is a stability limit for the weights that can be used for the artificial damping terms. This limit is actually connected to the magnitude of the amplification factor of the scheme modified with the artificial terms. To obtain the best convergence rates the implicit damping had to be the exact Jacobian of the explicit counterpart added to the right-hand-side. In case the second order damping is treated implicitly, equation (4) must be modified to include the added implicit terms: for instance, the ξ sweep implicit side will be

$$\left\{I+\Theta\Delta t\left(\delta_\xi\Lambda_\xi - \delta_\xi\left(((\sigma J^{-1})_{i+1,j,k}+(\sigma J^{-1})_{i,j,k})(\omega_{i,j,k}^{(2)}\delta_\xi J_{i,j,k})\right)\right)\right\} \tag{9}$$

This form maintains the tridiagonal nature of the Jacobian matrix.

When treating the fourth order damping implicitly, the differentiation of the Jacobian matrix brings about a scalar pentadiagonal system that can be written for the ξ sweep as

$$\left\{I+\Theta\Delta t\left(\delta_\xi\Lambda_\xi - \delta_\xi\left(((\sigma J^{-1})_{i+1,j,k}+(\sigma J^{-1})_{i,j,k})(\omega_{i,j,k}^{(4)}\delta_\xi^3 J_{i,j,k})\right)\right)\right\} \tag{10}$$

A brief set of tests on a straight channel geometry proved that the 4^{th} order implicit damping (eq. (10)) could bring a large gain in convergence rate with respect to the 2^{nd} order (eq. (9)). For a straight three-dimensional channel with approximately 10^4 points with an inlet-section-width to channel-length ratio of 15 (typical of internal flows geometries), the tridiagonal solver associated with equation (9) could be run at CFL=2 which gave the convergence history shown in figure 2(a), whereas the pentadiagonal solver associated with equation (10) proved to be much more robust and gave the much higher convergence rate shown in figure 2(b) with CFL=10. Despite an increase of around 25% in computational time to invert the pentadiagonal matrix with respect to the tridiagonal one, the implicit 4^{th} order option proved to be much faster and more robust, and was retained in all of the calculations.

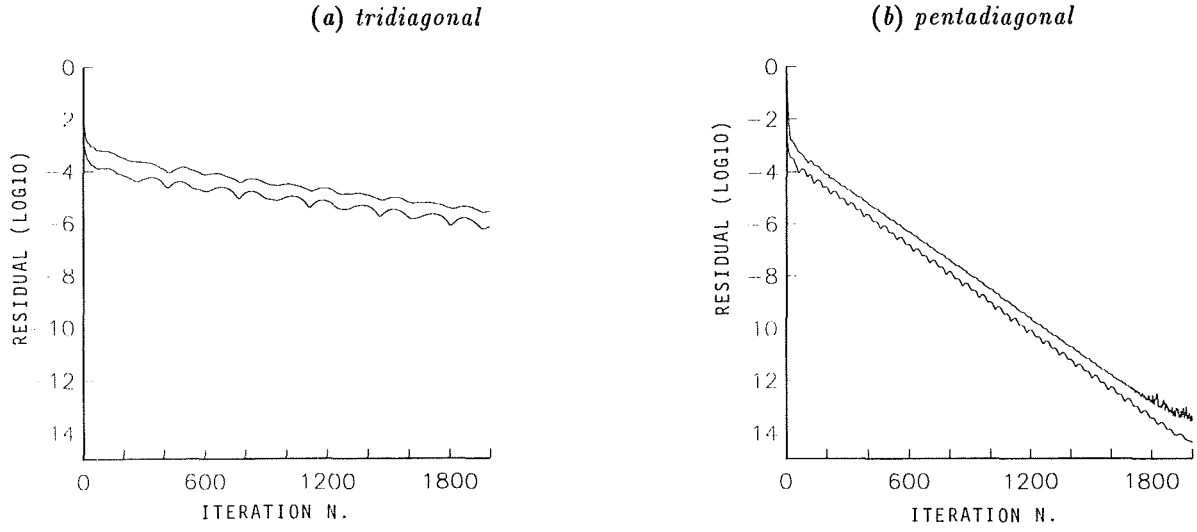

Figure 2. Convergence tests for tridiagonal or pentadiagonal solvers.

• Wall treatment of artificial damping.

It is well known that any kind of artificial damping term introduces an error that has to be minimized in order not to affect the solution heavily. Among the various approaches that can be found in the literature, the nonlinear damping formulation proposed by Jameson et al. (ref. 13) ensures that the second order terms are introduced only at shocks while keeping the fourth order in the smooth region of the computational domain. However, it is possible to prove that, if the presence of the boundaries is not properly accounted for when introducing the artificial terms, nonzero momentum and mass fluxes can be produced at the boundaries. This fact can be easily seen by considering figure 3. Figure 3(a) shows the fourth order damping weights applied at every single point i for the ξ direction. The fourth order difference stencil used here is

$$\delta^4_\xi(Q_{i,j,k}) = Q_{i-2,j,k} - 4\,Q_{i-1,j,k} + 6\,Q_{i,j,k} - 4\,Q_{i+1,j,k} + Q_{i+2,j,k}$$

The fourth order damping is normally switched off at i=1 and i=2 so that no special treatment at the wall is required. Figure 3(a) shows that, doing so, the sum of the fourth order damping weights for every locaton i is zero only in the internal flow field for $i \geq 5$. This ensures that no net fluxes are added only in the internal domain, while the sum of the artificial damping weights yields nonzero values for $1 \leq i \leq 4$. These weights actually correspond to a nonzero third order derivative centered at i=(2+1/2). The same procedure may be followed for the second order damping that is switched off at i=1 (figure 3(b)). The sum of the weights for every location i is zero only for $i \geq 3$. This yields a first order derivative centered at i=1/2, that corresponds to a first order flux at the wall. These flux errors can be easily controlled in two

dimensions by a grid refinement in the wall proximity where high gradients are expected. In three-dimensional internal flows we are forced to use coarser grids and the wall boundary condition is applied on very large surfaces with the result of possible large mass errors. To control the mentioned flux errors, a third order derivative, with the differencing stencil given by

$$\delta^3_\xi(Q_{i,j,k}) = -Q_{i-1,j,k} + 3\,Q_{i,j,k} - 3\,Q_{i+1,j,k} + Q_{i+2,j,k}$$

was added at i=2 to balance the fourth order damping weight. The same procedure was followed to balance the second order damping at the wall where a first order derivative, with the differencing stencil given by

$$\delta_\xi(Q_{i,j,k}) = -Q_{i-1,j,k} + Q_{i,j,k}$$

was added at i=2.

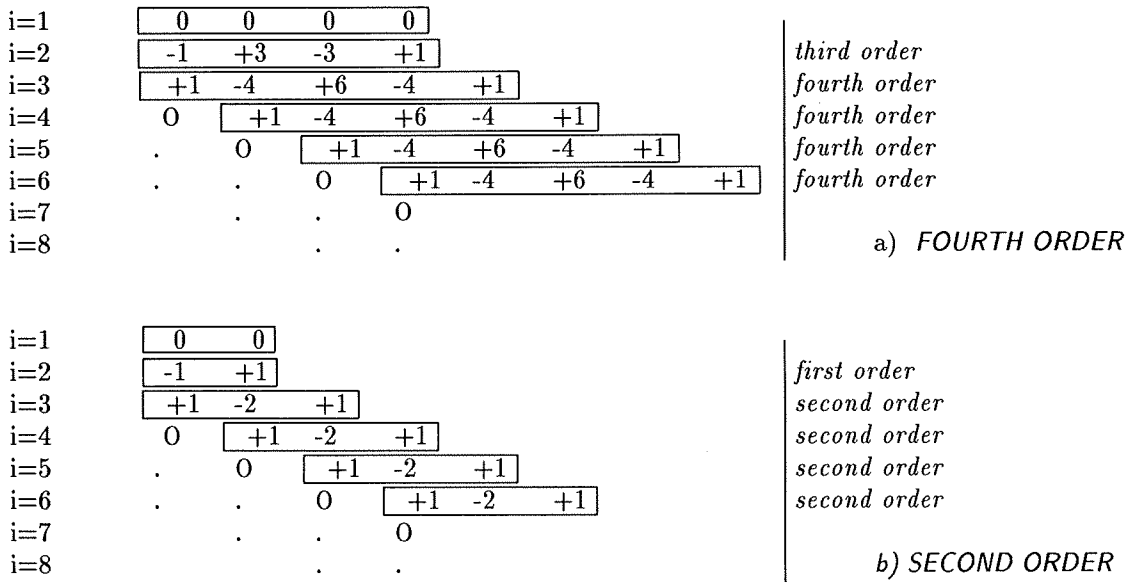

Figure 3. Artificial dissipation treatment at boundaries.

TURBULENCE MODELS

Baldwin-Lomax for Multiple Boundaries

The standard version of the Baldwin-Lomax (ref. 4) zero-equation turbulence model was implemented here. This two-layer model divides the flow field into an inner layer close to the wall, in which viscous effects are dominant, and an outer layer. The influence of the solid wall is damped according to the Van Driest exponential function.

This algebraic turbulence model was originally developed for a single boundary layer, but in three-dimensional internal flows the presence of multiple boundaries causes the interaction of more than one

boundary layer. Whereas the inner, or viscous layer, is driven by what happens on the closest wall only, for the outer layer an averaging procedure is necessary to account for the various wall effects. In the present set of calculations three approaches have been examined to account for the presence of more than one boundary layer.

• Wall Treatment 1
Only the geometrically closest wall is considered to compute the outer viscosity without any averaging.

• Wall Treatment 2
The inner layers are driven by the closest wall only, whereas the viscosity in the outer layer is computed with a simple weighted average according to the inverse of each wall distance as follows

$$\mu_{t,outer} = \frac{1}{\sum_{w}^{n} \frac{1}{W_w}} \sum_{w}^{n} \left(\frac{\mu_{t,outer}^{w}}{W_w}\right)$$

where W_w is the wall distance, w is the wall number, and N is number of walls present in a cross section.

• Wall Treatment 3
In case only one boundary layer is present, the Van Driest damping succeeds in modeling the wall effect. Starting from this standpoint, the inner layer viscosities are computed using only the closest wall contribution, while the viscosity in the outer layer is computed as a simple weighted average according to the inverse of the value of the Van Driest damping expression for each wall.

q-ω two-equation Model

In a previous investigation, Michelassi (ref. 7) found that the low-Reynolds number forms of the two-equations models, like k-ϵ, could give accurate prediction of two-dimensional incompressible separated flows. Unfortunately, these forms were found to be numerically stiff, mainly on account of the correction terms introduced to model the low-Re effects that necessitate a strong mesh refinement in the sublayer. Furthermore, an initial profile for the turbulent quantities has to be specified consistently to start the calculations. A first attempt to implement the Chien's and the Rodi's two-layer low-Reynolds number forms of the k-ϵ model did not bring any converged result mainly because of difficulties in specifying both a sufficient mesh refinement and proper initial profiles for complex three-dimensional flows. Coakley (ref. 15), reassembling the Jones and Launder low-Reynolds-number form of k-ϵ model, proposed the q-ω two-equation model, in which the effect of molecular viscosity is directly modelled: This formulation ensured better numerical behavior as compared with other low-Re formulations. This vector form of the model transport equations rewritten in our notation is (ref. 19)

$$\frac{\partial \overline{Q}}{\partial t} + \frac{\partial \overline{E}}{\partial \xi} + \frac{\partial \overline{F}}{\partial \eta} + \frac{\partial \overline{G}}{\partial \zeta} = \frac{\partial \overline{E}_v}{\partial \xi} + \frac{\partial \overline{F}_v}{\partial \eta} + \frac{\partial \overline{G}_v}{\partial \zeta} + \overline{H} \tag{11}$$

in which $\overline{H}$ stands for the sink and source terms vector. The full definition of the flux vectors can be found in reference 19. The two transported quantities, q and ω, are related to the more familiar k and ϵ via the following relations:

$$q = k^{1/2} \quad ; \quad \omega = \epsilon \; / \; k \tag{12}$$

It is important to observe that ϵ appearing in equation (12) is the isotropic part of the dissipation rate; this quantity does not account for any nonisotropic effect (for example, the presence of a wall) and

tends to zero on solid boundaries. (Conversely, the total dissipation rate tends to a finite value related to the wall shear stress.) This choice allows ω to be used as an unknown since, assuming that both k and ϵ are going to zero at the wall with the same slope, ω tends to a finite value.

q-ω Solution

The two transport equations for q and ω are implicitly solved by using the same algorithm given in equation (1). The two equations are solved in a sequential manner and decoupled from the flow variables mainly because the coupling is provided only by the coefficients of the diffusive terms and the sink and source terms. Because of this choice, the scalar three-diagonal algorithm was implemented for the turbulence model solution. The only difference with respect to the solution of the N-S equations is the presence of the sink-source vector $\overline{\overline{H}}$ in equation (11). This term can be included in the three sweeps:

$$\begin{aligned}
&[\, I+\Theta\Delta t\left(-H_j\, c_\xi + \delta_\xi A - \delta_\xi^2 A_v\right)]* \\
&[\, I+\Theta\Delta t\left(-H_j\, c_\eta + \delta_\eta B - \delta_\eta^2 B_v\right)]* \\
&[\, I+\Theta\Delta t\left(-H_j\, c_\zeta + \delta_\zeta C - \delta_\zeta^2 C_v\right)]*\Delta Q = RHS
\end{aligned} \tag{13}$$

where the same definitions given for equation (1) hold with the only addition to the Jacobian being the sink and source terms, H_j, that are weighted in the three sweeps according to c_ξ, c_η, c_ζ, and $c_\xi+c_\eta+c_\zeta= 1$. This Jacobian is computed neglecting the contribution of the damping function D. Its form for the two q and ω equations is

$$H_j^q = \frac{\partial H^q}{\partial(\rho J^{-1} q)} = \frac{1}{2}\frac{C_\mu DS}{\omega} - \frac{1}{3} P_d - \frac{\omega}{2}$$

$$H_j^\omega = \frac{\partial H^\omega}{\partial(\rho J^{-1}\omega)} = -\frac{2}{3} C_1 D P_d - C_2\, 2\omega$$

in which S and P_d are production terms (ref. 19). In place of their exact form, Coakley (ref. 15) proposes an approximation of the Jacobians based on the turbulent viscosities that should ensure the dominance of the main diagonal. Figure 4 shows the comparison of the convergence rates of every single variable obtained without any sink or source terms Jacobian, with the exact Jacobian, and with Coakley's approximation in a typical internal flow geometry. Surprisingly, there is no big gain in introducing the Jacobian in the implicit side of the operator since with the three formulations it was always possible to obtain the same residual reduction in 300 iterations. The choice of the sweeps in which the two Jacobians H_j^q and H_j^ω are introduced is not important. The error introduced in the approximate factorization of the implicit side of equation (13) increases roughly a factor proportional to H_j when introducing the Jacobian in the three sweeps, thereby choosing $c_\xi=c_\eta=c_\zeta= 1/3$: this has only a weak influence on the convergence rate. Nevertheless, in the present calculations typically the best convergence rates have been obtained by using $c_\xi=0$, $c_\eta=0.5$, and $c_\zeta=0.5$, where ξ is the main flow direction and η and ζ are the fine grid directions.

Although physical evidence shows that the turbulent kinetic energy k is zero at solid walls, the boundary condition for ϵ, and consequently ω, is less evident. For the q-ω model, Coakley (ref. 15) found it convenient to impose a zero-normal derivative at the wall; this condition was retained in the present calculations.

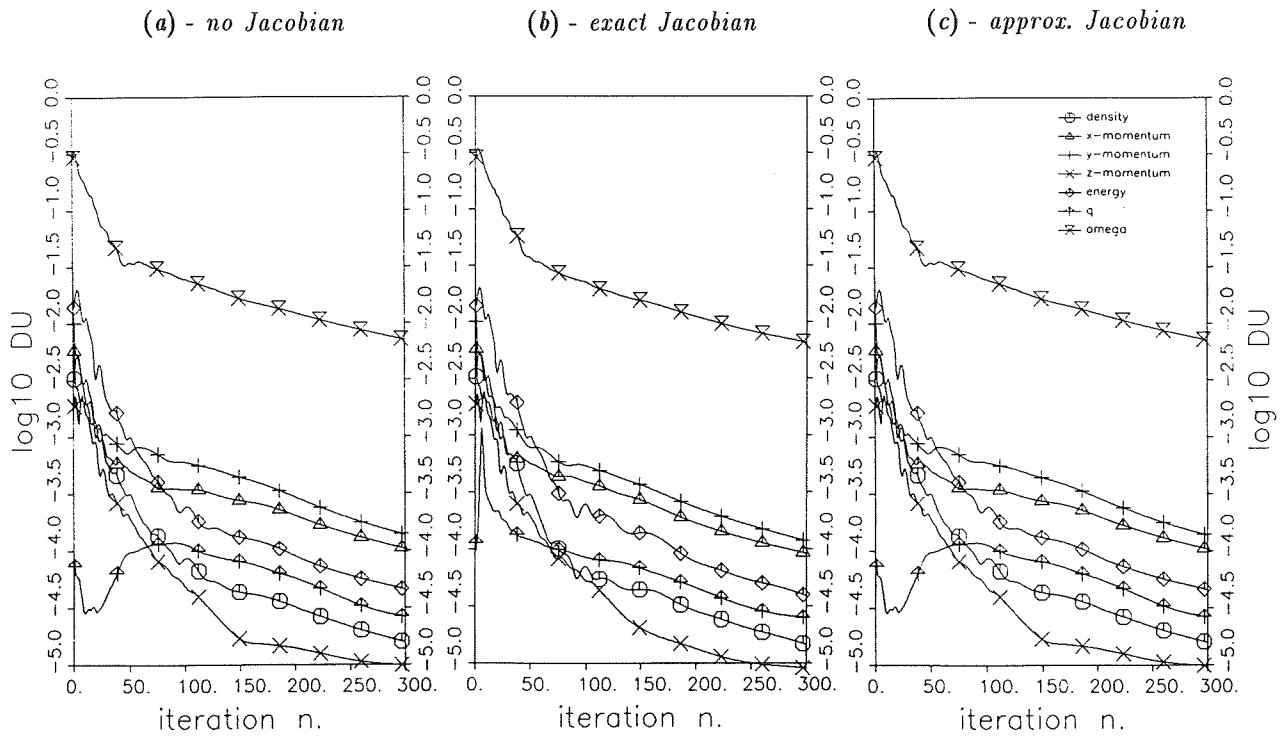

Figure 4. Convergence tests for implicit treatment of q-ω sink-source terms.

RESULTS

Incompressible S-duct

A first validation of the code was performed by computing the flow in an S-duct with a constant area cross section. The measurements (ref. 16) were taken for an incompressible fluid (water). The S-duct is given by two 22.5° bends with 4-cm hydraulic diameter and 28-cm mean radius of curvature. This geometry was regarded as an interesting test since flow passages with similar shapes are often used to redirect the flow for air intakes in aeronautical engines. The efficiency of such ducts may be heavily affected by the presence of secondary flows so that the ability of a code to detect secondary velocities is essential for a proper depiction of the flow pattern.

The sketch of the flow domain is shown in figure 5. Since the geometry and the flow were symmetric with respect to the x-r plane, it was possible to study only one-half of the duct by imposing a symmetric boundary condition on the same plane. For the laminar flow regime, the Reynolds number, Re, based on the inlet bulk velocity, Ub, and hydraulic radius was 790. The grids employed for this calculation are shown in figure 6. The coarser grid (figure 6(a)) has $70\times29\times15$ points with a ratio between two consecutive grid cells in the cross flow directions of 1.1, and the refined one (figure 6(b)) has $80\times59\times30$ points with the same stretching ratio in the cross flow plane. The fluid adopted in the experiments is water so that, in order to have negligible compressibility effects, the isentropic Mach number was set equal to 0.1 (which gives the inlet total pressure, outlet static pressure ratio) to ensure minor density changes.

The flow pattern and the growth of the secondary motions is mainly pressure driven because of the very smoothly bending walls that cause no flow separation. Still, this kind of flow necessitates a very accurate prediction of the boundary layer, even in laminar regime, otherwise the secondary flows may be incorrectly predicted or completely lost. Figure 7(a) shows the measured (circles) and computed velocity profiles with the two grids mentioned above (dashed line is the coarser grid; solid line is the refined grid) for the 5 sections (indicated in fig. 5) on the symmetry plane reported in the experiments. The slight discrepancies in the computed velocities with the two grids at section 1, where the double-S starts, may be

attributed to the thinner boundary layer predicted with the refined grid that produced a flatter velocity profile. Nevertheless, the agreement with experiments is fairly good. The agreement does not deteriorate for sections 2, 3, and 4 in both the coarse and refined grids. Section 5 clearly shows that the secondary motions could not be predicted by the coarse grid, whereas they are fairly well reproduced by the refined one. This behavior is thought to be independent of the grid points in the main flow direction, (as it will be demonstrated in a further test) in which only 10 points are added in the refined grid, and it is closely related to the poor resolution of the boundary layer provided by the coarse grid in which the cross-flow momentum diffusion is clearly overestimated.

Figure 7(b) shows the velocity profiles for the midspan section (r=1/2) at the same five sections. Basically the same comments given for the symmetry plane could be repeated here for the first three sections, whereas on section 4 and 5 agreement deteriorates in proximity of the symmetry plane. This may be attributed to the poor grid quality close to the symmetry plane, but also to the fact that in the calculations a zero gradient condition was imposed in the direction normal to that plane, whereas experiments show that the velocity gradient is far from being zero on the same plane for section 4. The typical computed secondary motion pattern at the exit of the second bend is shown in figure 7(c): The complex flow pattern exhibits two counter-rotating vortices in proximity of the two curved walls.

Nearly 1500 iterations were necessary to reach an averaged residual of the order of 10^{-5} on the refined grid, but typically less than half of these iterations were necessary to obtain the same residual with the coarser grid. These calculations were performed with an early version of the code where only the second order implicit damping was implemented so that the slow convergence rate may be attributed to both the small Mach number and to the small CFL number that could not exceed 2 without encountering stability problems.

The turbulent flow regime was run at the experimental condition of Re=40.000. For this calculation, it was necessary to provide a more stretched grid at the wall, so that the 80×59×30 grid was reassembled with a point expansion ratio in the cross flow directions equal to 1.3. This provided the necessary point clustering at the boundaries to describe the thin boundary layer and allowed the first point at the wall to be placed at $y^+ \approx 2$. For this test case, the Baldwin-Lomax model was implemented with wall treatment 1 (see section on Baldwin-Lomax for multiple boundaries).

Figure 8(a) shows the set of measured and computed velocity profiles on the symmetry plane for the same five cross sections given in figure 5. For this flow configuration the agreement is reasonably good, especially at cross sections 4 and 5 where the pressure gradients induce a strong secondary motion that seems to be correctly predicted by the present solver insofar as the agreement with measurements does not deteriorate as the second bend exit is approached and the secondary velocities reach their maximum. The momentum transfer to the external part of the second bend, particularly evident in sections 4 and 5, is reproduced well since the computed velocity profile asymmetry seems to be in close agreement with experiments.

Figure 8(b) shows the computed and measured velocities on the midspan plane along the duct. The agreement is again good for the five sections and better than that found for the laminar flow regime mainly because the measured velocity profiles exhibit a zero gradient on the symmetry plane that is correctly modelled by the symmetry condition imposed on the x-r plane. Still, at sections 3 and 4 the kink in the velocity profile close to the wall is not correctly predicted.

The static pressure coefficient in the main flow direction, defined as

$$C_p = \frac{p - p_{inlet}}{\frac{1}{2} \rho U_b^2}$$

is shown figure in 8(c) at three different locations (z=0,r=0), (z=0,r=1), and (r=1/2,z=1/2). The agreement is generally good. The pressure trend is correctly predicted together with the head loss.

Figure 8(d) shows the convergence history obtained with CFL=2: For this calculation the same early version of the code mentioned previously was used. The solid upper line refers to the maximum residual, and the dashed one refers to the averaged residual; the spikes present in the first curve correspond to the updating of the turbulent viscosity performed every five iterations. It is remarkable that the pressure distribution did not change after the first 500 iterations, whereas to get the correct velocity profiles, it was found necessary to reach a residual of the order of 10^{-5} to 10^{-6}.

Stanitz Elbow

The flow in the accelerating rectangular elbow with 90° turning and variable cross section described by Stanitz (ref. 17) has been computed with an inviscid version of the code and with both the Baldwin-Lomax and q-ω turbulence models. This test case was selected since it provides a good set of measurements including wall pressure distribution and visualization of secondary flows at the elbow exit section. The shape of the elbow was analytically computed by Stanitz to give no separation with a strong area reduction and a specified pressure distribution on the side wall under incompressible flow conditions. A sketch of the experimental setup is shown in figure 9. The flow and the elbow geometry are symmetric with respect to the x-y midspan plane thereby allowing a zero normal gradient condition. Among the various flow conditions investigated in reference 17, we selected the one with M_{exit}=0.4 and with no spoiler at the duct inlet with a thin initial boundary layer.

- Inviscid Calculations

A first set of tests was performed with an inviscid version of the code. The convergence characteristics of the scalar form of the approximate factorization could be tested for inviscid calculations where the necessity of accounting for the diffusive terms on the implicit side of equation (4) drops. Only the pressure distribution on the walls of the elbow was compared with measurements in this set of calculations: no attempt was made to specify an experimental inlet profile of total pressure that was kept flat. The inlet boundary condition was specified extrapolating the Riemann invariant from the first section inside the duct (ref. 18). Two grids were used: a 25×15×11 grid and a 50×15×11 grid with constant grid spacing in the cross-flow directions. The grid point locations in the streamwise direction were made to coincide with the points supplied by Stanitz (ref. 17) for the description of the elbow geometry with the addition of three cross sections at the outlet to allow the use of a zero gradient condition.

Figure 10 shows the qualitative static pressure and Mach number isolines on the symmetry plane of the elbow. The small wiggles visible at the domain exit are due to the very small 4^{th} order damping weight that was set equal to $\Omega^{(4)}$=1/256, together with $\Omega^{(2)}$=0. The small value of the fourth order damping weight is allowed by the very coarse grid in the cross flow direction that automatically introduced a numerical diffusion. Despite the very coarse grids implemented here, the static pressure distribution p_s, defined as

$$P_s = \frac{p - p_{exit}}{p_{total} - p_{exit}}$$

shown in figure 11, reveals a fairly good agreement with experiments. Although the pressure drop position is located correctly for the two grids on both the side and symmetry planes, the kink in the static pressure distribution on the suction surface at the side wall could not be reproduced since it is caused by the presence of secondary flows. The pressure distribution appears to be independent of secondary flows induced by viscous effects until the first part of the bend is reached. The local pressure rise located at S=2 (where S is the streamwise coordinate along the centerline) is introduced by the growth of secondary velocities and is totally lost by the inviscid solver. The solution proved also to be fairly grid independent, at least to the grid refinement in the main flow direction: No additional tests were performed to verify the influence of the point distribution in the cross-stream direction.

The implicit treatment of 2^{nd} and 4^{th} order artificial damping was compared using the 50×15×11 grid. Figure 12 shows the comparison between the two implicit damping schemes; the solid line refers to the 2^{nd} order implicit damping with $\Omega^{(2)}=1/4$, and the dashed line refers to the 4^{th} order implicit option with $\Omega^{(4)}=1/256$. The gain in convergence rate is remarkable; in fact, the fourth order solver could be run at CFL=10, whereas the second order one could not be run at CFL≥5. Any further increase of the artificial damping weights gave slower convergence histories. Unfortunately the same convergence rate is not obtainable for viscous calculations because of the strong point clustering and viscous effects not exactly accounted for on the implicit side of the operator.

• Viscous Calculations

The viscous calculations in turbulent flow regime were performed on the five grids summarized in table I. The use of various point clustering and distribution allowed a comprehensive investigation on the mesh dependence of the calculations. With this set of grids it was possible to verify the influence of the grid points number in the main flow direction, with 51 or 99 points, and the cross flow direction with 31×21 and 41×31 points with expansion ratios of 1.2 and 1.3. The refined grid (number 5) shown in figure 13 adopts the same distribution of points in the main flow direction that was used for the refined grid in the inviscid calculations and which allowed placing the first grid point at the wall at $y^+\approx 1$. The Reynolds number, Re, based on the total conditions at the inlet section is approximately $2.5\cdot 10^{+6}$.

grid number	points	expansion ratio
1	50x31x21	1.2
2	50x41x31	1.2
3	99x31x21	1.2
4	50x31x21	1.3
5	51x41x31	1.3

Table I. Grids for viscous calculations on Stanitz elbow.

These calculations were mainly aimed at the proper prediction of the wall pressure distribution that is heavily affected by the growth of secondary velocities and a qualitative comparison of the secondary flows predicted by the Baldwin-Lomax zero-equation model and the q-ω two equation model. The choice of the experimental spoilerless configuration allowed the turbulence models to be compared for a very thin boundary layer that required a heavy point stretching at the wall. Regarding the inlet boundary condition, in the Baldwin-Lomax model the inlet turbulent viscosity was extrapolated from inside the domain, and in the q-ω model a flat turbulent kinetic energy profile with various turbulence levels was specified at the inlet section while ω was extrapolated from inside the domain.

The first set of tests concerns the Baldwin-Lomax model with the different wall treatments mentioned. With the experimental total pressure profile specified at the inlet section, the computed static pressure profiles are compared with the measurements in figure 14. The plots refer to the static pressure distribution in the section corners on the side wall and the symmetry plane. It is evident that the way the outer viscosity is computed may play a significant role in the correct prediction of the pressure distribution. Wall treatment 1, in which only the closest wall is considered, and 2, in which the outer turbulent viscosity is weighted according to the inverse of the wall distance, do not show large changes even if the two approaches are considerably different. For both techniques, the agreement with experimental results is fairly good on the pressure side of both the side wall and the symmetry plane. The suction side on both planes shows that the static pressure is overestimated. This is probably due to the presence of computed secondary flows much stronger than the experimental ones. The computed pressure drop induced by the presence of the bend and the strong flow acceleration is smoother than the measured one: This phenomena

is caused by high turbulent viscosities that induce a heavy momentum diffusion in the cross-flow direction followed by a static pressure redistribution and growth of the boundary layer thickness. The agreement with measurements improves with the turbulent viscosities averaging given by wall treatment 3. No big changes between the multiple wall treatments are found for the pressure side of both the side wall and the symmetry plane where it was always possible to have accurate results. Differences start to appear on the suction side where multiple wall treatment 3 shows the closest agreement with experiments. Still the pressure minimum located at S=2, where velocities on the cross section start to develop, is not captured. This test suggests that the averaging technique based on the Van Driest damping expression for the mixing length can give reasonable predictions. All of the computations with the Baldwin-Lomax model were performed with multiple wall treatment 3.

The results of the mesh dependence tests for the Baldwin-Lomax model are summarized in figure 15, where the computed static pressure distribution in the four corners of the cross sections using different grids are compared with measurements. The pressure distribution profiles show that there are practically no differences between the predictions obtained with grids 1 and 3. This proves that an increment of the grid points number in the main flow direction does not produce any gain in terms of accuracy: This is strictly connected to the boundary layer resolution that is not improved by using grid 3. The growth of secondary flows is influenced by the low momentum regions located close to the wall, the correct simulation of which is not ensured by the two grids. Conversely, the implementation of grid 2 clearly improves the accuracy of the results. The static pressure profile on the suction side of the side wall is in better agreement with experiments than the pressure distributions given by grids 1 and 3. It is worthwhile observing that the use of a more refined grid in the cross flow direction shows that the computed pressure minimum on the suction side is correctly located, even if its value is still overestimated, whereas this local minimum, located approximately at S=2, is completely lost with the other two grids. Nevertheless, the static pressure distribution on the symmetry plane appears to be weakly affected by grid refinement. No further investigation was performed by varying the cross-flow points expansion ratio.

The flow simulation with the q-ω model required more tests since it was necessary to investigate both the dependence on the mesh refinement and on the inlet turbulence level. The use of grids with expansion ratios equal to 1.2 did not ensure significant improvements in results since not enough points were located close to the wall. In order to have a reasonable definition of the turbulent kinetic energy peak at the wall, the grid expansion ratio was fixed at 1.3. The results of the first set of tests are summarized in figure 16 in which, adopting the coarse grid 4, the inlet turbulence level was changed to verify its influence on the static pressure distribution. Even when the inlet turbulence level is decreasing from 5.0% to 0.1%, the computed profiles progressively approach the measurements, the predictions are still far from experiments for the suction side of both the symmetry plane and the side wall. This indicates the presence of a large momentum diffusion that is possibly caused by insufficient mesh refinement or too high turbulence level, or both. Figure 17 shows the results obtained with grid 5 and lower turbulence levels. Figures 16 and 17 show that the refined grid with the same turbulence level brings some improvement of the agreement with experiments, proving that the coarser grid was largely inadequate for this flow configuration (see, for instance, the 0.1% level). The growth of the secondary flows is evident in figure 17 where the static pressure distribution computed with the inviscid approach is compared with the results of the two-equation model obtained with different turbulence levels.

The direct comparison of the turbulent calculations with the inviscid computation, in which the same pressure distribution is found on both the side wall and the symmetry plane because of the absence of secondary motions, shows large differences on the suction side only starting from S=2 where experiments deviate from the inviscid solution. The 1% turbulence level, not reported in figure 17, appeared to bring still a too high momentum diffusion so that this level was progressively decreased from 0.5% to 0.1%. The static pressure distribution on the pressure wall is mainly driven by convective phenomena, whereas the distribution on the suction wall is largely influenced by diffusion processes: this is the reason why the pressure side distribution is always reproduced well and is nearly independent of the inlet turbulence level. The final result obtained with grid 5 and a 0.1% turbulence level shows a fairly good agreement with experiments on both the suction and pressure sides and seems to reproduce quite correctly the location and

the influence of secondary flows.

The predicted pressure distributions obtained by the Baldwin-Lomax model with wall treatment 3 and the q-ω model are very similar, but the two-equation model proved to be marginally more accurate especially on account of the static pressure distribution on the suction side. Figure 18 shows that the two models predict approximately the same static pressure pattern on the symmetry plane with nearly the same pressure drop due to the acceleration of the flow. Still, from figure 19, where the Mach number isolines are shown on the same symmetry plane, it is possible to observe that the zero equation model predicts a slightly thicker boundary layer than the one predicted with the q-ω. These differences start immediately after the inlet section and become more evident as the exit section is approached. This indicates a different turbulent viscosity distribution in the wall region. The Baldwin-Lomax model was in fact found to predict a sharper growth of the turbulent viscosity in the wall region: still the two models gave comparable values of the turbulent viscosity in the flow core. The differences in the boundary layer thickness are evident in figure 20 where the velocities in the exit section of the channel are plotted. Although both the turbulence models show the same flow pattern, the two-equation model predicts the center of the secondary recirculation closer to the wall than that predicted by the zero-equation model in which the location of the center appeared to be in better agreement with experiments. This confirms a weaker cross-flow momentum diffusion given by the two-equation model as compared with the zero-equation model. This is caused by the aforementioned differences in the turbulent viscosities. It is remarkable that both formulations predict a small secondary vortex in the wall corner of the suction and pressure walls.

An interesting qualitative comparison of the predicted and measured secondary flows is given by figure 21. Figure 21(a) shows the experimental flow visualization by injecting a smoke filament inside the boundary layer close to the side wall at the inlet section of a reduced model of the channel. The low-momentum particles located well within the boundary layer are bent towards the suction wall by the pressure gradients, but the high-momentum particles exhibit a weaker turning. Figure 21(b) shows the secondary flow predicted by the zero equation model, and figure 21(c) refers to the results obtained with the q-ω model. From this comparison it is evident that the zero-equation model predicts a smoother turning of the velocities which is in slightly better agreement with the experimental picture than the q-ω model.

A typical total pressure loss distribution on the channel exit section is given in figure 22. The results computed with the Baldwin-Lomax model and grids 1 and 2 show the much thicker boundary layer obtained with the coarser grid. The refined grid ensures a correct description of secondary flows together with the location and magnitude of the total pressure losses.

Concerning computational details, with the present research version of the code, 6000 sec were necessary to perform 2500 iterations with the q-ω turbulence model with a 63.550-point grid on a Cray Y-MP supercomputer, which ensured an overall residual of the order of 10^{-6}, whereas a reduction of approximately 30% in CPU time could be obtained by using the zero-equation model. As mentioned by Coakley (ref. 15), the q-ω model was found to be remarkably insensitive to the initial field specified to start the calculations for q and ω. In the present tests it has always been possible to start the model with a flat distribution of the turbulence quantities. For the viscous calculations it was found to be good practice to keep CFL$<$10 together with 1/32 as the weight for the fourth order artificial damping. The total absence of shocks allowed the second order artificial damping to be eliminated in all calculations. Moreover, the aforementioned wall treatment of the fourth order damping ensured inlet-outlet mass errors of the order of 0.5%.

CONCLUDING REMARKS

The scalar form of the approximate factorization coupled with a turbulence model proved to be suitable for solving turbulent internal flows where diffusive terms play a dominant role. The introduction of an approximate treatment of the diffusive terms proved to increase convergence of the algorithm for internal flow configurations. Nevertheless, the implicit treatment of these terms must be tested for a wider range of geometries and Reynolds numbers. The influence of Mach number on convergence rate needs to be

investigated especially for the proposed approximate implicit treatment of diffusive terms based on a space derivative of the fluid density: New tests are currently being performed.

For the Stanitz elbow geometry the Baldwin-Lomax turbulence model proved to give results in acceptable agreement with experiments provided that the presence of multiple boundaries is properly accounted for. The low-Re q-ω two-equation model version investigated here proved to be suitable for three-dimensional computations and gave a satisfactory description of the flow field with a manageable number of grid points and only a small increase of computational time with respect to the algebraic model.

ACKNOWLEDGMENTS

The first author would like to express his gratitude to ICOMP and the Internal Fluid Mechanics Division of NASA Lewis Research Center for providing facilities and computer time for this work.

REFERENCES

1. T.H. Pulliam, L. Steger. "Implicit Finite Difference Simulations of Three-Dimensional Compressible Flows," *AIAA Journal, Volume* 18, *N.*2, *February* 1980.

2. A. Ballantyne, C. J. Knight, J. C. Kreatsoulas, D. Lee. "Experimental/Computational Study of Viscous Flow in a Contracting Rectangular Elbow," *AIAA Journal, Volume* 26, *N.* 12, *December*, 1988.

3. J. W. Yokota. "A Diagonally Inverted LU Implicit Multigrid Scheme for the 3-D Navier-Stokes Equations and a Two Equation Model of Turbulence." NASA CR-182209, 1988.

4. B. S. Baldwin, H. Lomax. "Thin Layer Approximation and Algebraic Model for Separated Turbulent Flows." *Proceedings AIAA* 16th *Aerospace Sciences Meeting*, 1978.

5. R. V. Chima, J. W. Yokota. "Numerical Analysis of Three-Dimensional Viscous Internal Flows." NASA TM-100878, 1988.

6. C. E. Towne. "Computation of Viscous Flow in Curved Ducts and Comparison with Experimental Data." NASA TM-83548, 1984.

7. V. Michelassi. "Testing of Turbulence Models with an Artificial Compressibility Solution Method." Report SFB (Sonderforschungsbereich, University of Karlsruhe) 210 T49, University of Karlsruhe, Karlsruhe, West Germany, January, 1989.

8. F. Martelli, V. Michelassi. "An Implicit Factored Solver for Inner Turbulent Flows," *Proceedings AIAA/ASME/SAE/ASEE* 24th *Joint Propulsion Conference, July* 1988.

9. W. Rodi. "Recent Development in Turbulence Modelling," *Proceedings* 3rd *Symposium on Refined Flow Modelling and Turbulence Measurements, July*, 1988.

10. T. H. Pulliam. "Efficient Solution Methods for The Navier-Stokes Equations," Von Karman Institute For Fluid Dynamics, Lecture Notes on Numerical Techniques for Viscous Flows Calculations in Turbomachinery Bladings, Bruxelles, January 1986.

11. R. M. Beam, R. F. Warming, "Implicit Numerical Methods for the Compressible Navier-Stokes and Euler equations," Von Karman Institute For Fluid Dynamics, Lecture Notes on Computational Fluid Dynamics, Bruxelles, February 1982.

12. T. H. Pulliam, D. S. Chaussee, "A Diagonal Form of an Implicit Approximate-Factorization Algorithm." *Journal of Computational Physics, N.* 39, 1981.

13. A. Jameson, W. Schmidt, E. Turkel. "Numerical Solutions of the Euler Equations by Finite Volume Methods Using Runge-Kutta Time-Stepping Schemes." *AIAA* 14th *Fluid and Plasma Dynamics Conference, July* 1981.

14. T. H. Pulliam. "Artificial Dissipation Model for the Euler Equations." *AIAA Journal, Volume* 24, *N.*12, 1986.

15. T. J. Coakley. "Turbulence Modeling Methods for the Compressible Navier-Stokes Equations." *Proceedings AIAA* 16th *Fluid and Plasma Dynamics Conference, July* 1983.

16. A. M. K. P. Taylor, J. H. Whitelaw, M. Yianneskis. "Developing Flow in S-Shaped Ducts, I- Square Cross-Section Duct." NASA CR-3550, 1982.

17. J. D. Stanitz, W. M. Osborn, J. Mizisin. "An Experimental Investigation of Secondary Flow in an Accelerating Rectangular Elbow." NACA TN-3015, 1953.

18. R. V. Chima. "Development of an Explicit Multigrid Algorithm for Quasi-Three Dimensional Viscous Flows in Turbomachinery." NASA TM-87128, 1986.

19. V. Michelassi, M.-S. Liou, L. A. Povinelli. "Implicit Solution of Three-Dimensional Internal Turbulent Flows." NASA TM-103099, 1990.

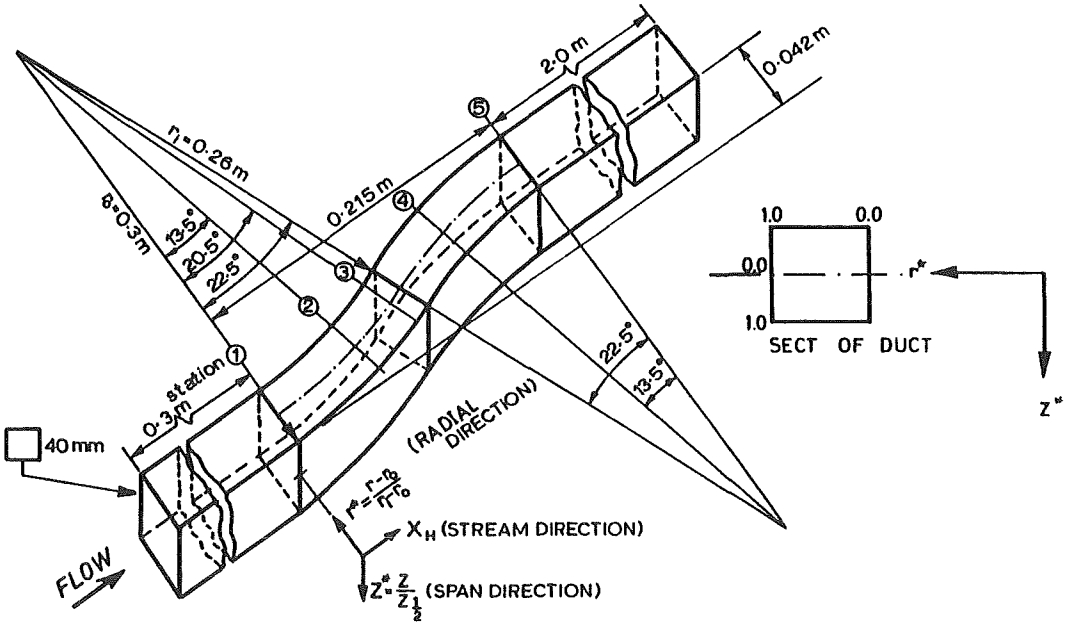

Figure 5. S-duct: Sketch of experimental setup.

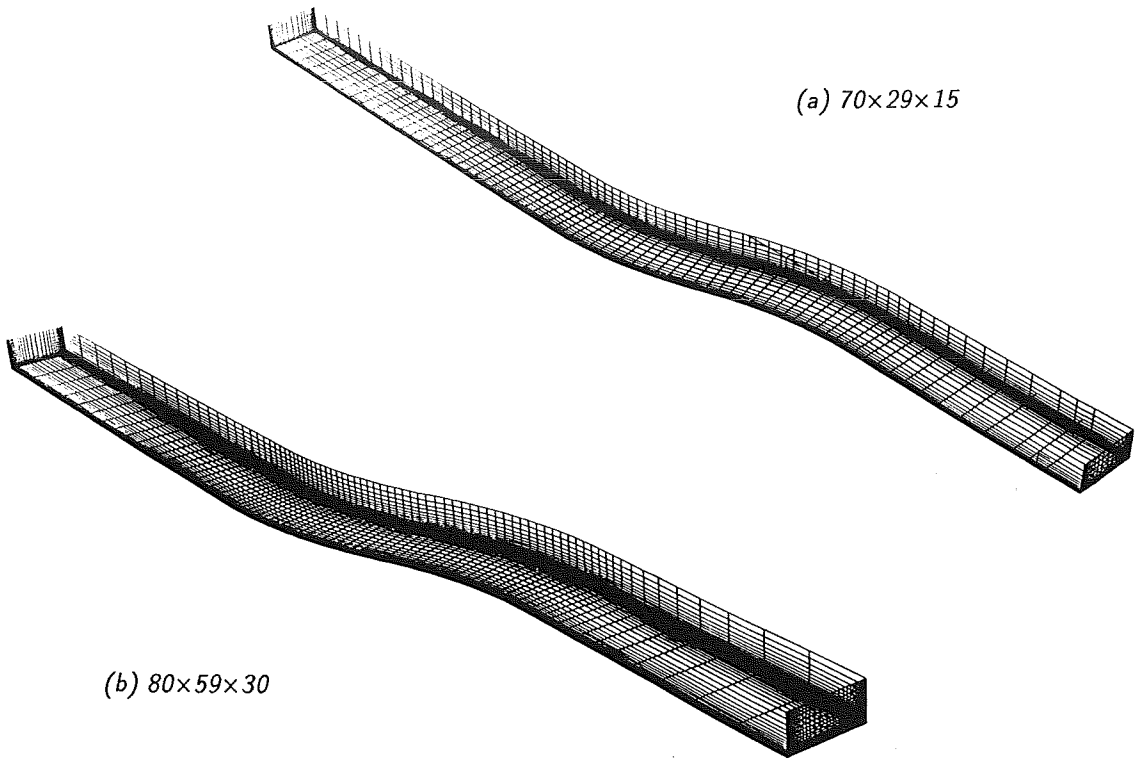

Figure 6. S-duct: Computational grids.

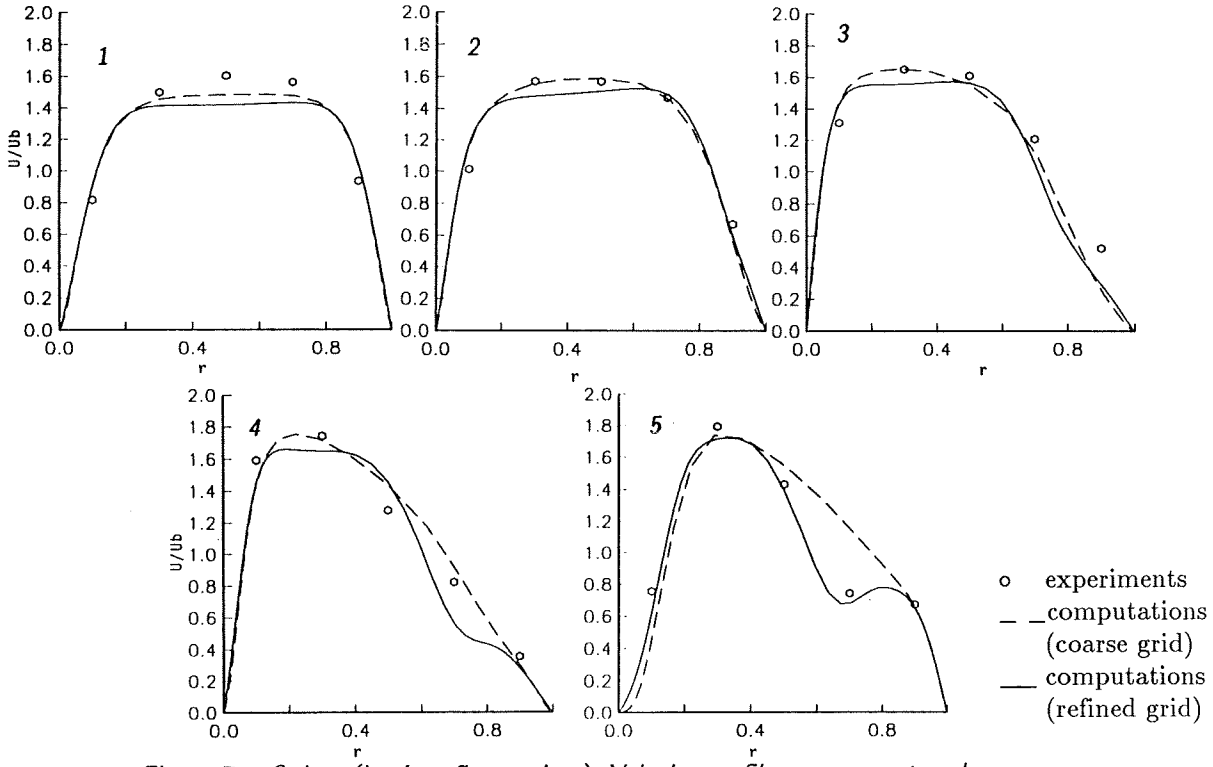

Figure 7.a. S-duct (laminar flow regime): Velocity profiles on symmetry plane.

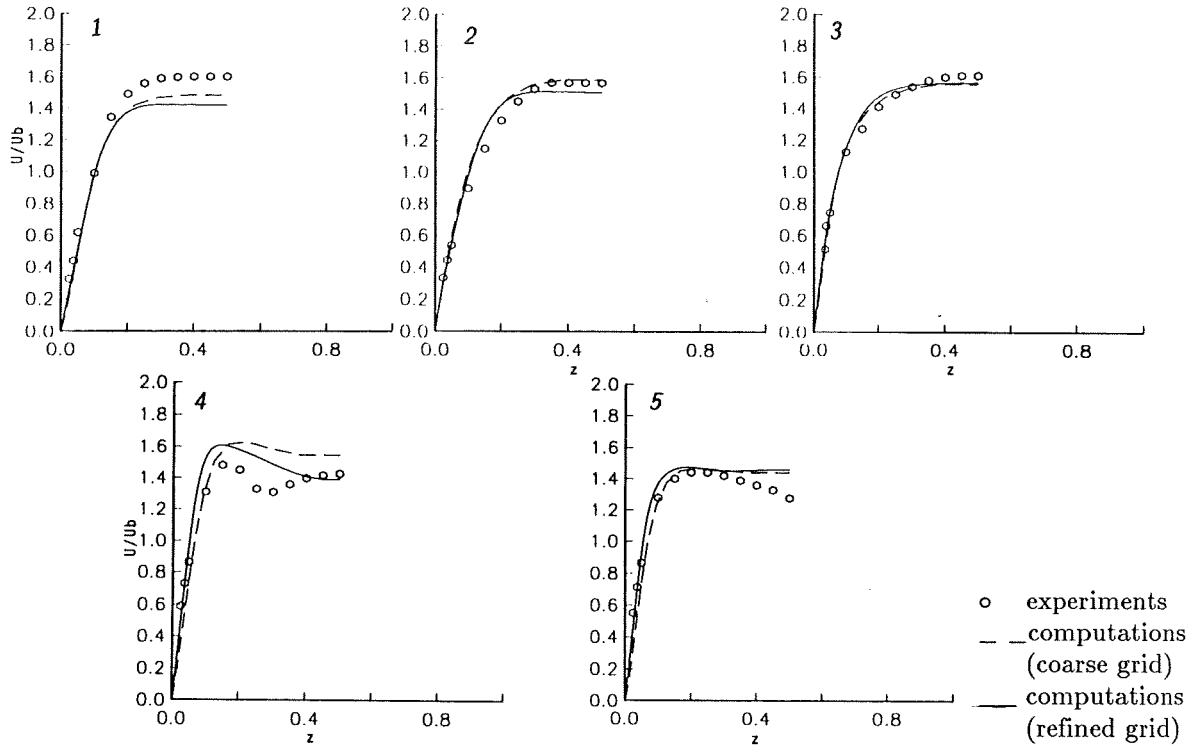

Figure 7.b. S-duct (laminar flow regime): Velocity profiles on midspan.

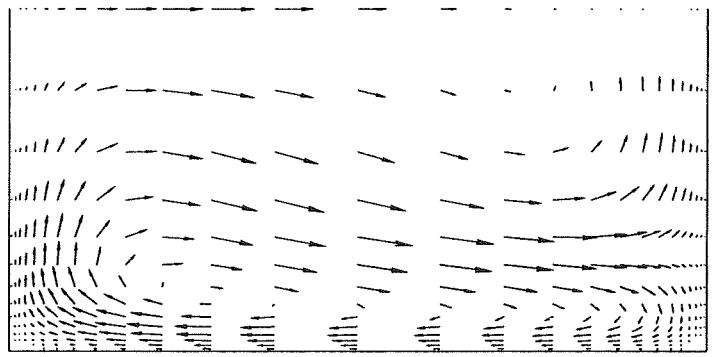

Figure 7.c. S-duct (laminar flow regime): Secondary velocity at bend exit.

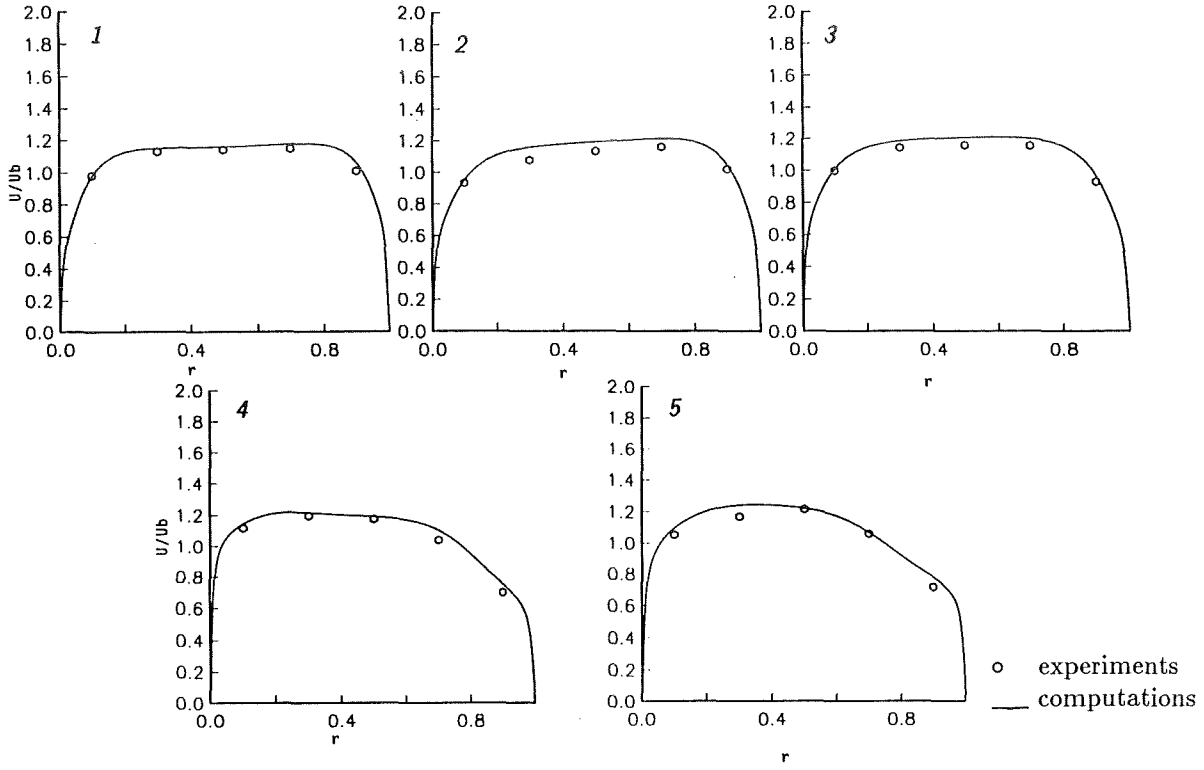

Figure 8.a. S-duct (turbulent flow regime): Velocity profiles on symmetry plane.

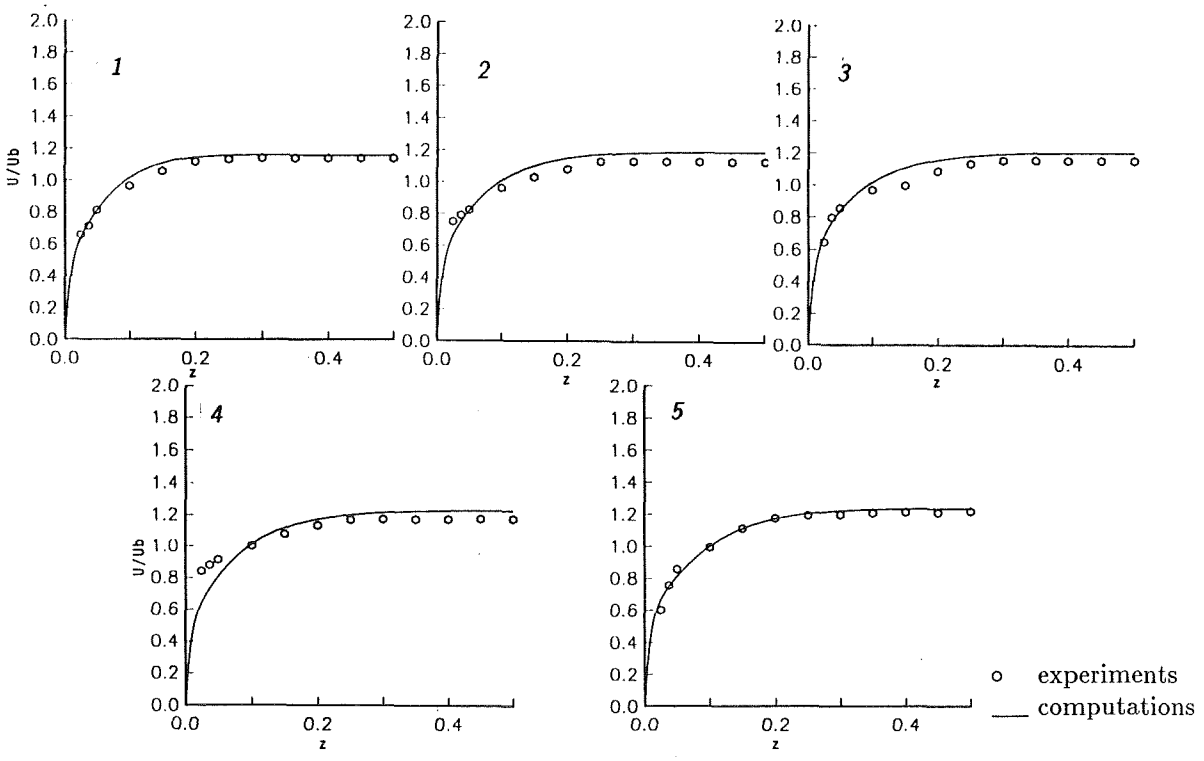

Figure 8.b. S-duct (turbulent flow regime): Velocity profiles on midspan.

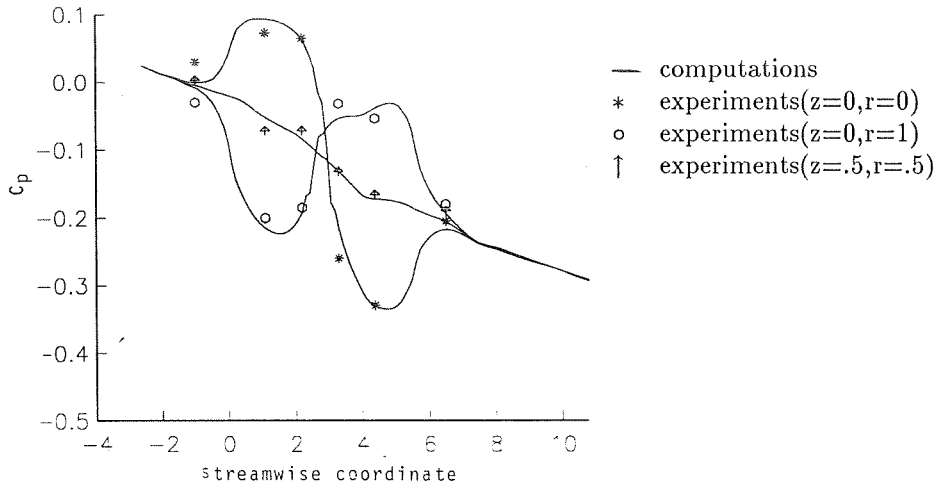

Figure 8.c. S-duct (turbulent flow regime): Wall C_p distribution.

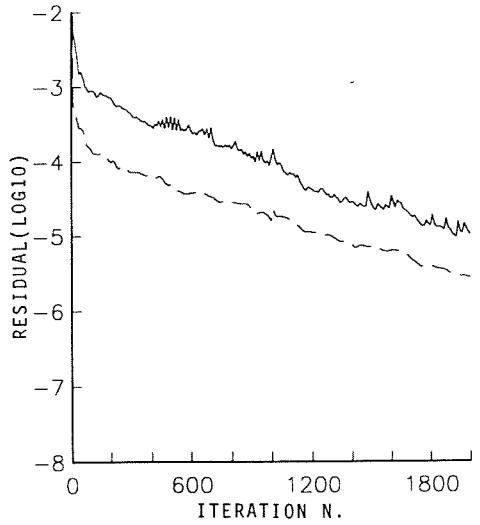

Figure 8.d. S-duct (turbulent flow regime): Convergence history.

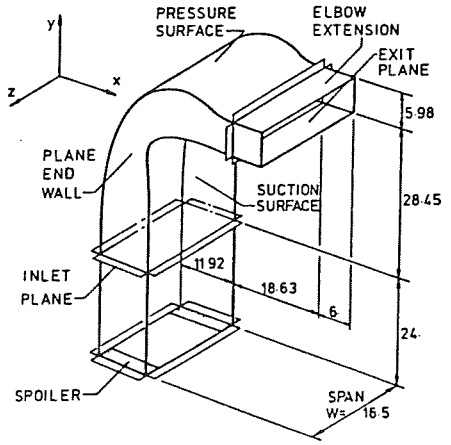

Figure 9. Stanitz elbow: Sketch of experimental set-up.

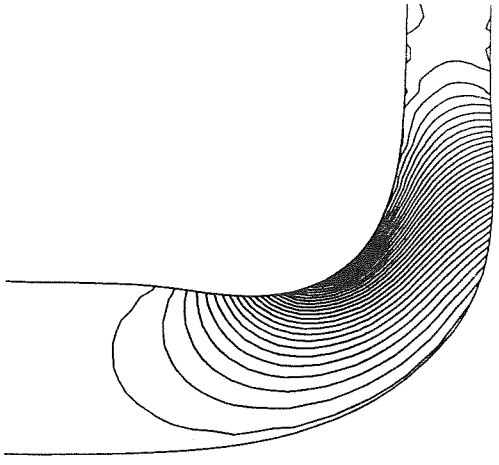

Figure 10.a. Stanitz elbow: Inviscid pressure isolines.

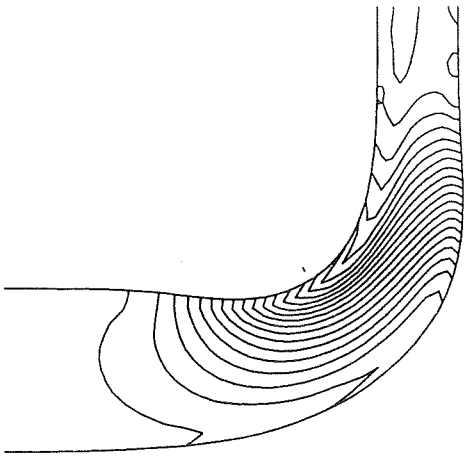

Figure 10.b. Stanitz elbow: Inviscid Mach number isolines.

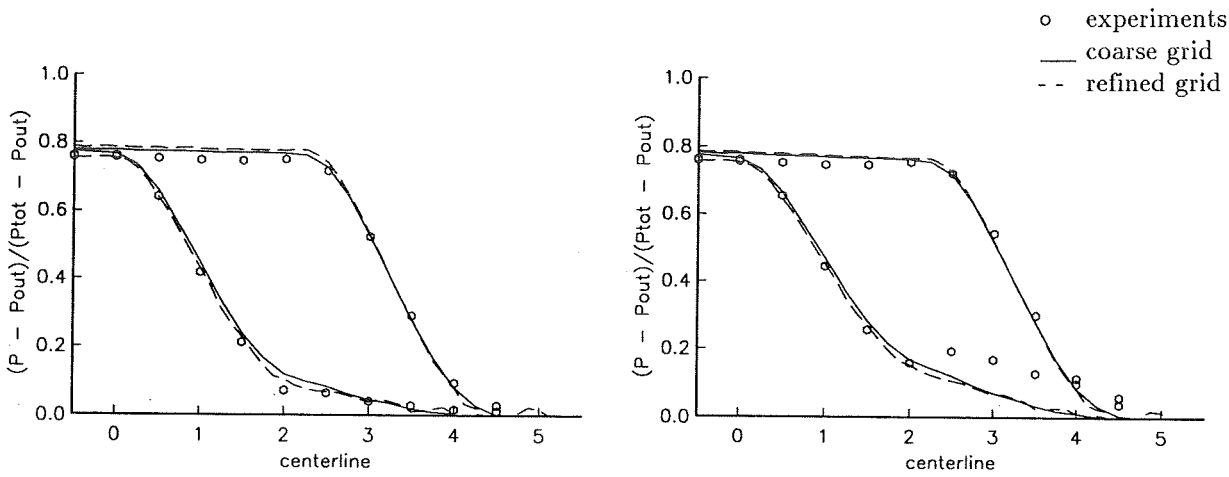

Figure 11. Stanitz elbow: Inviscid C_p distribution.

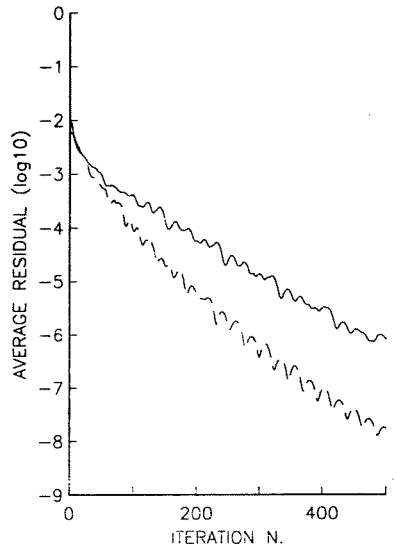

Figure 12. Stanitz elbow: Convergence history.

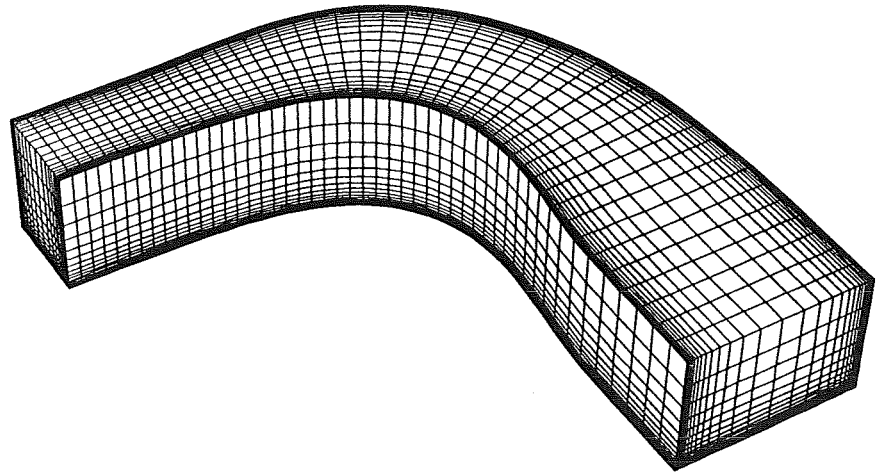

Figure 13. Stanitz elbow: Refined 50×41×31 grid.

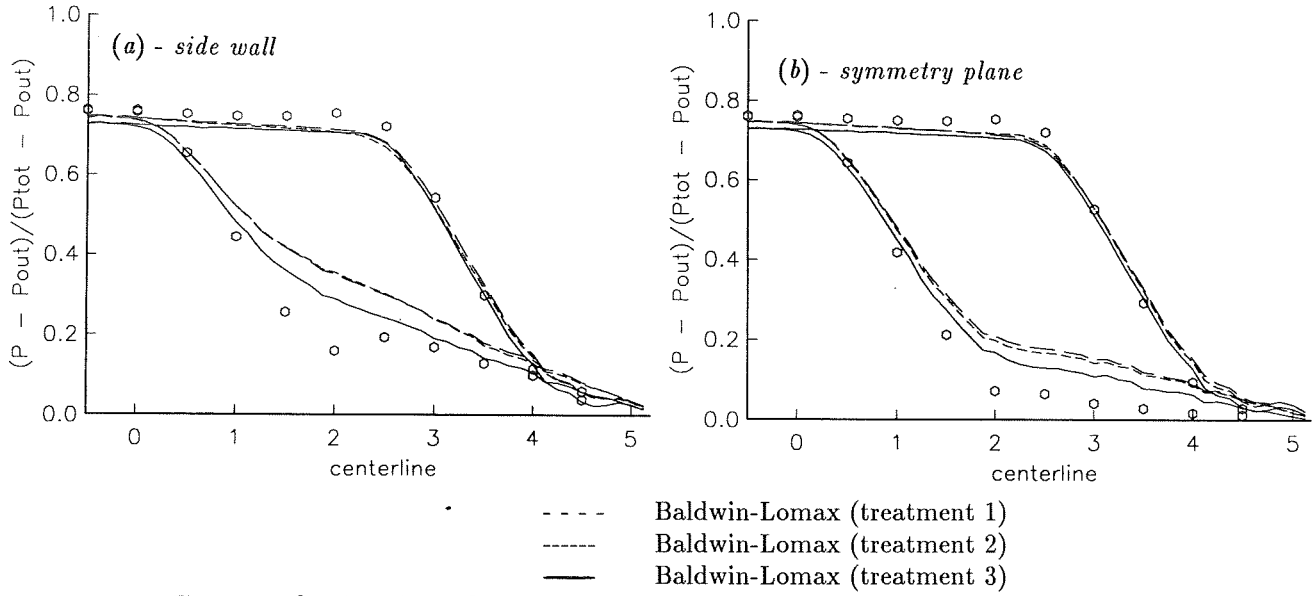

Figure 14. Stanitz elbow: C_p distribution with multiple wall treatments by Baldwin-Lomax model.

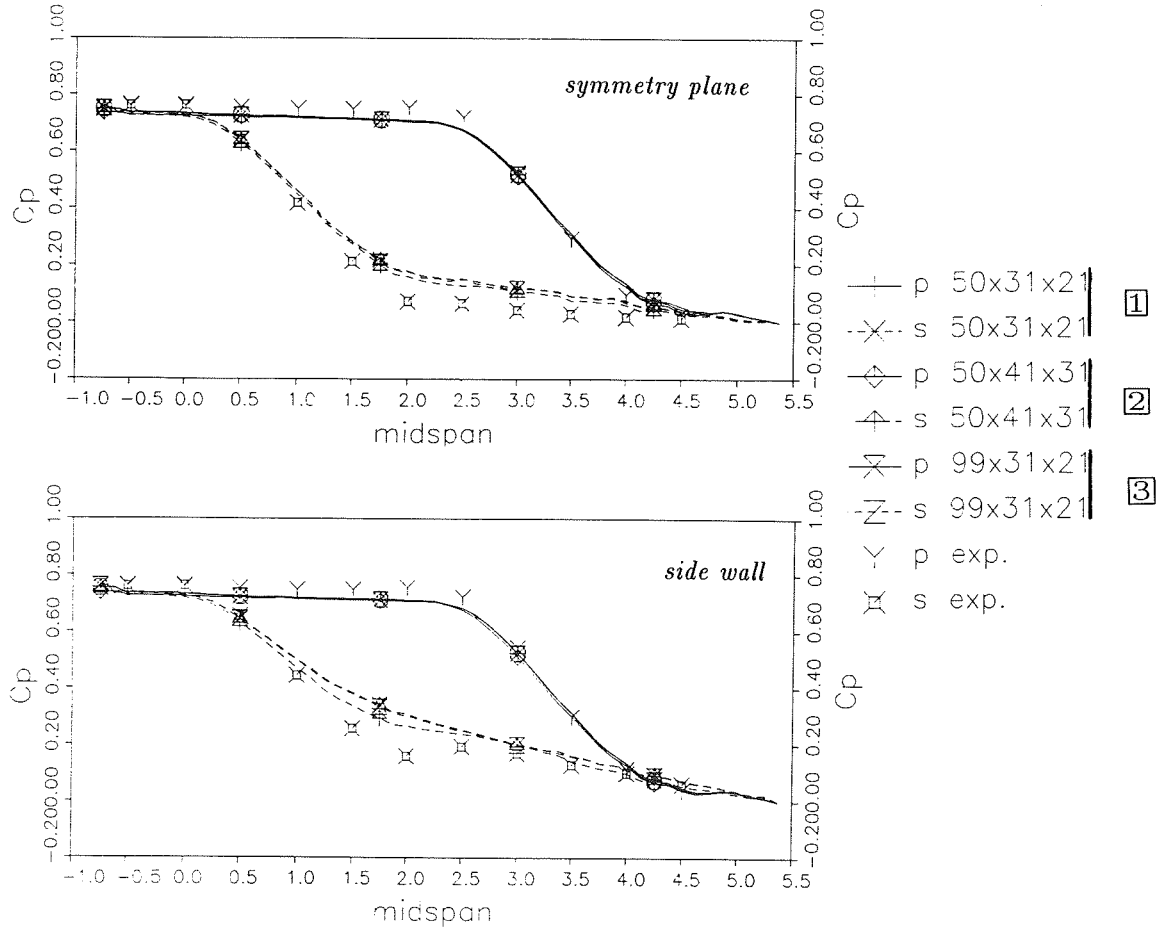

Figure 15. Stanitz elbow: C_p dependence on grid points by Baldwin-Lomax model.

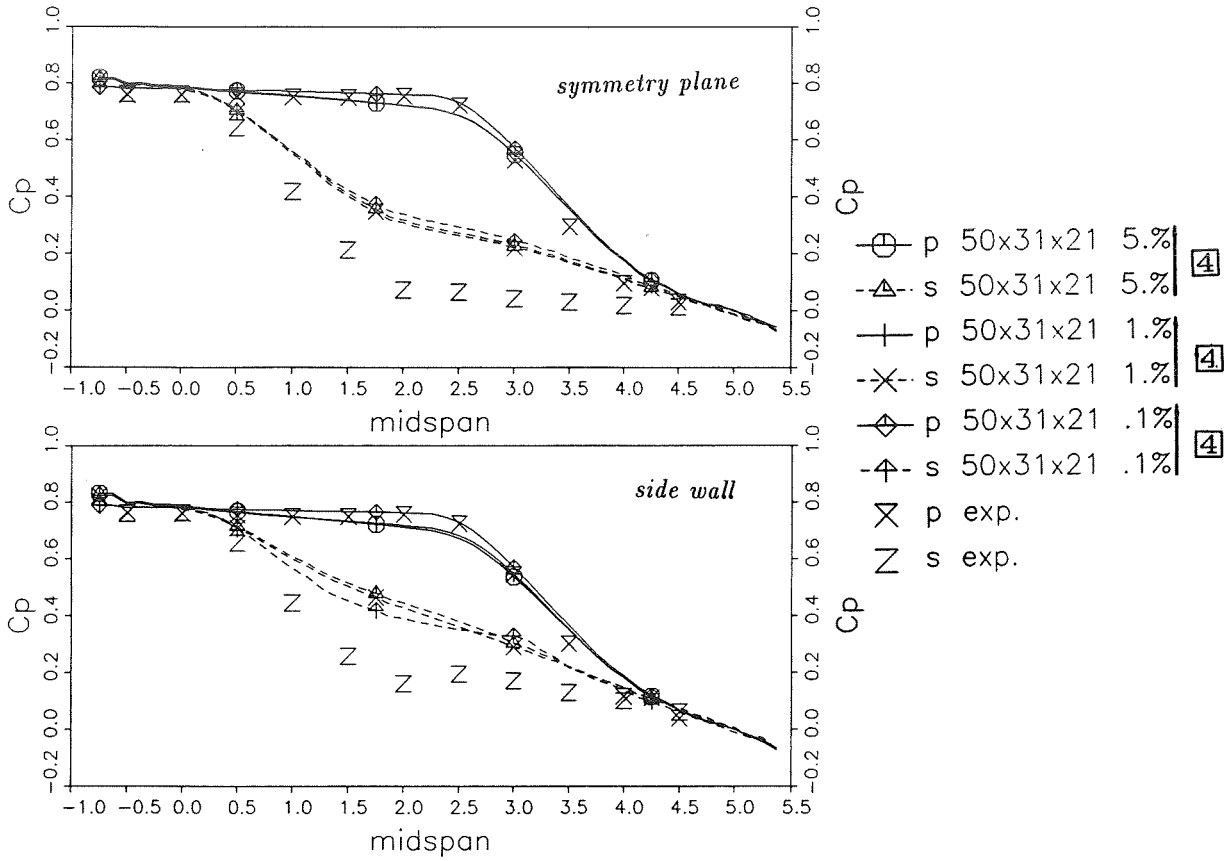

Figure 16. Stanitz elbow: C_p dependence on turbulence level by q-ω model (coarse grid).

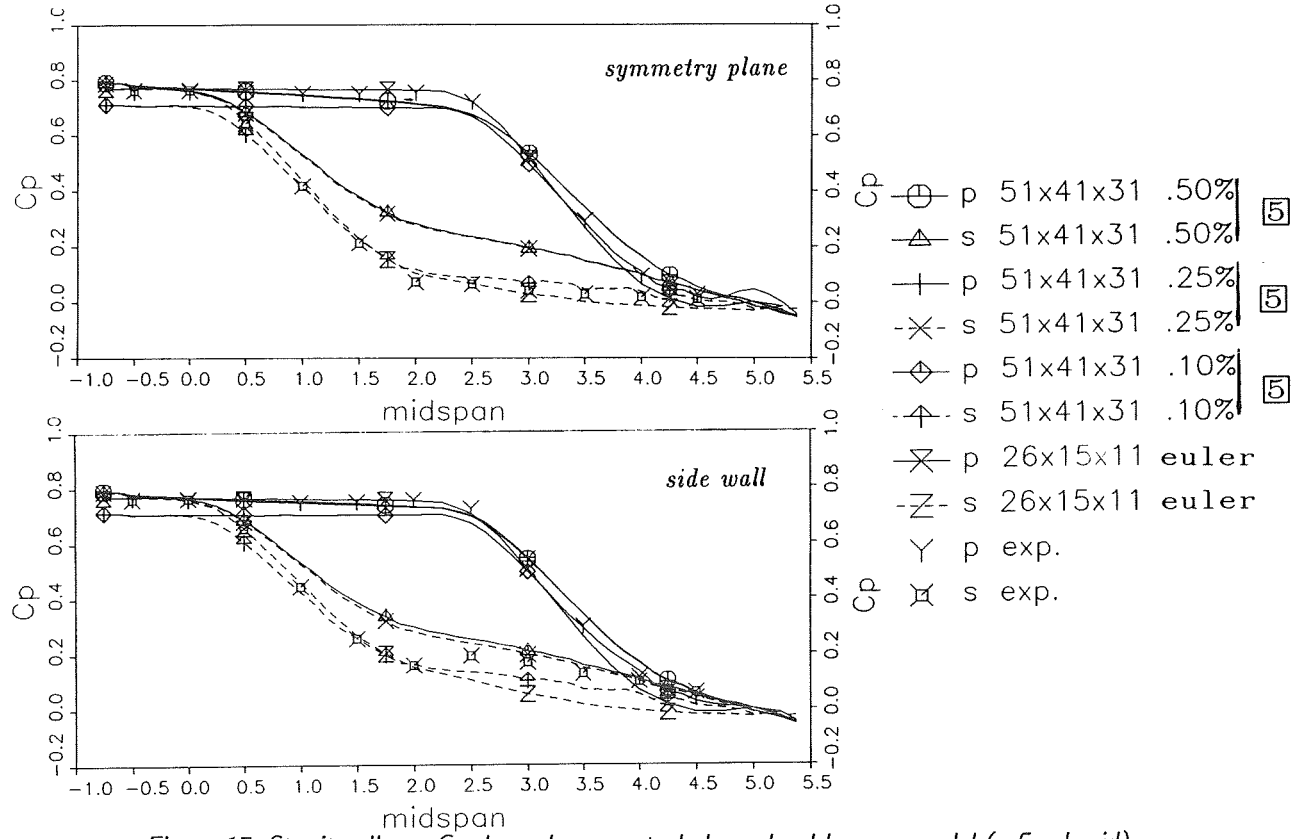

Figure 17. Stanitz elbow: C_p dependence on turbulence level by q-ω model (refined grid).

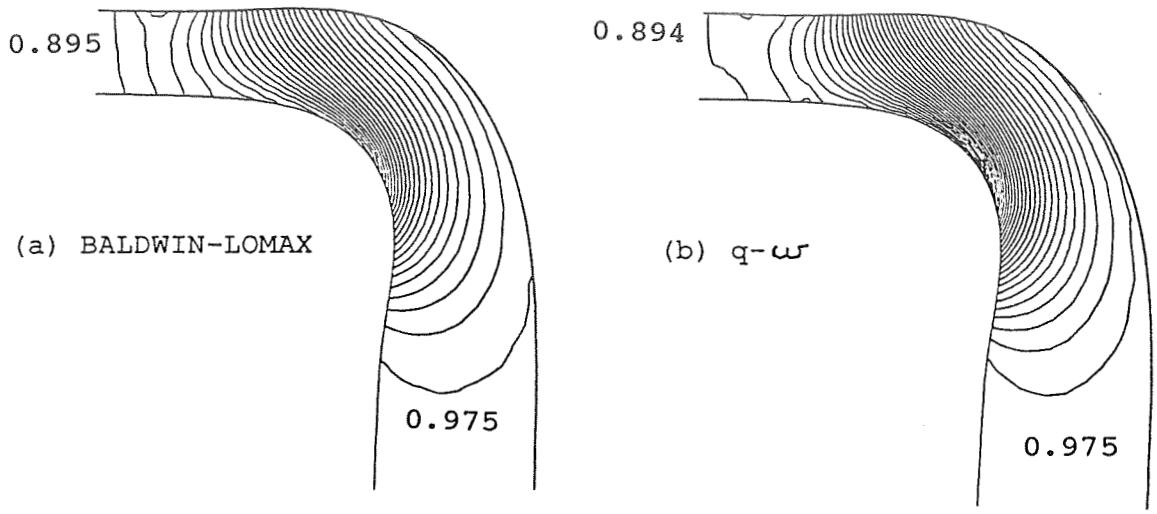

Figure 18. Stanitz elbow: Static pressure isolines on symmetry plane.

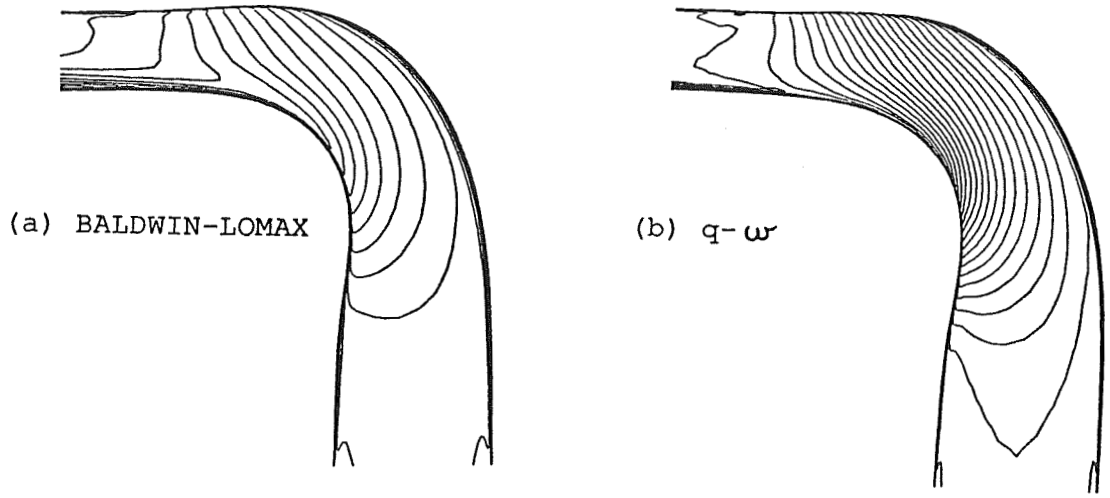

Figure 19. Stanitz elbow: Mach number isolines on symmetry plane.

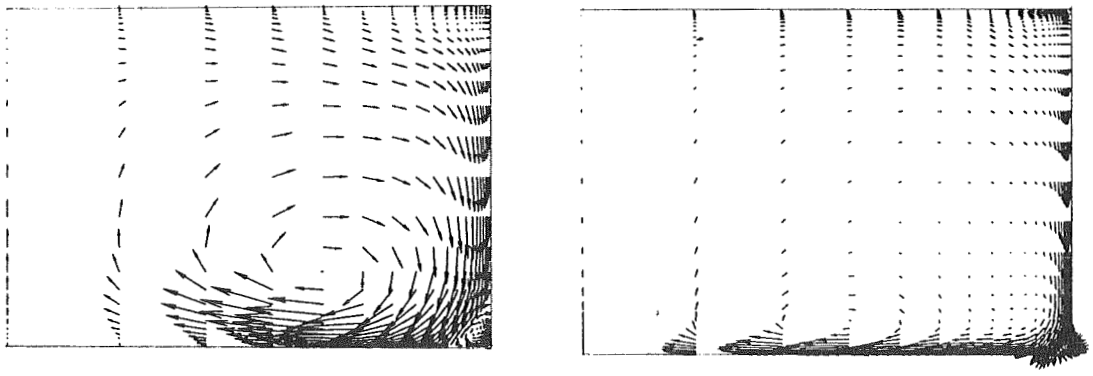

(a) Baldwin-Lomax (b) q-ω

Figure 20. Stanitz elbow: Velocity vectors at exit section.

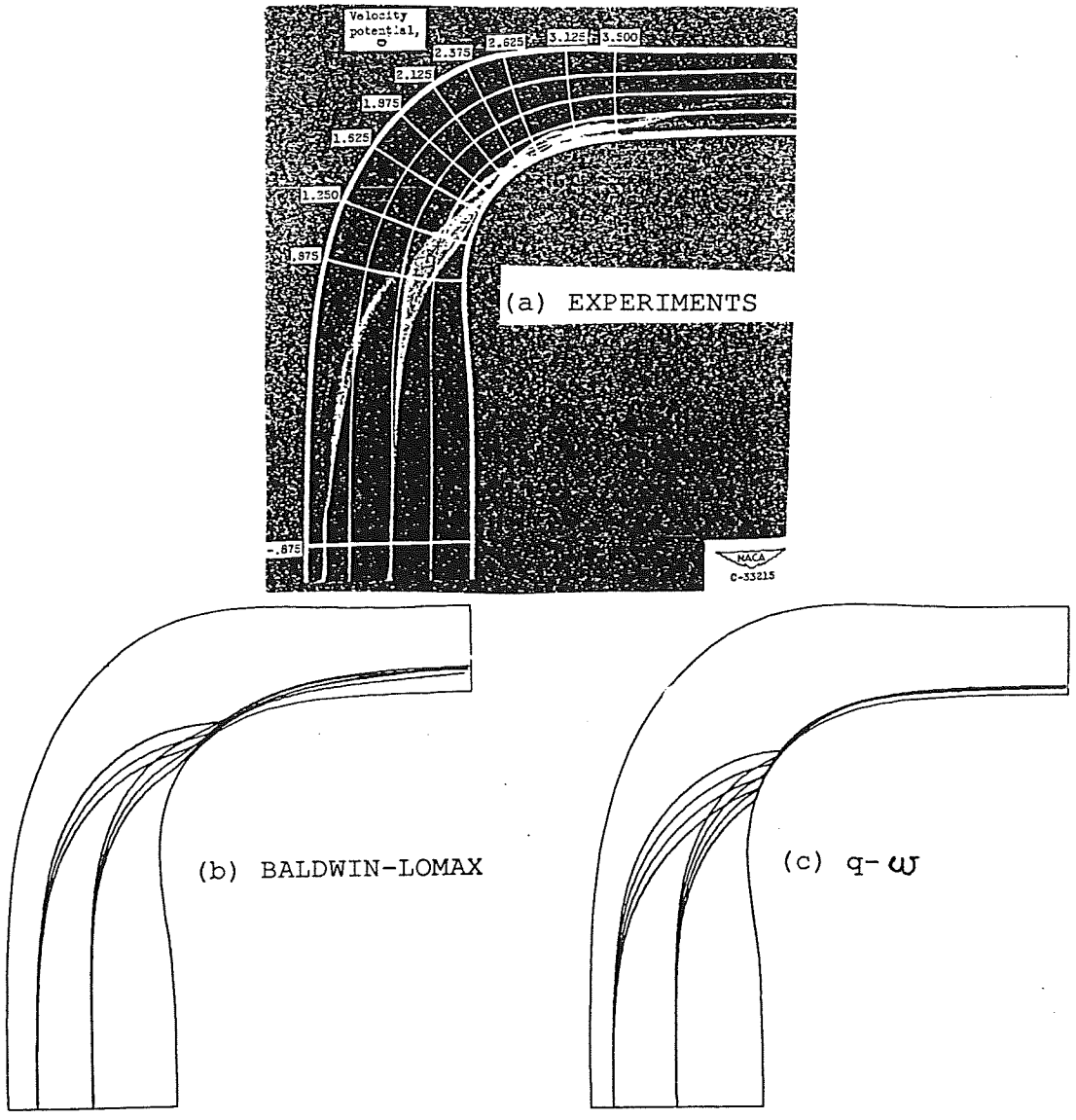

Figure 21. Stanitz elbow: Secondary flows visualization.

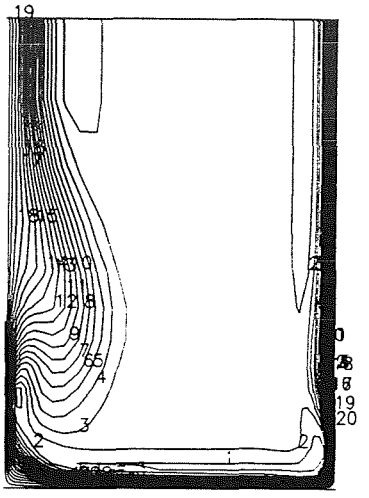

computations (51×31×21)

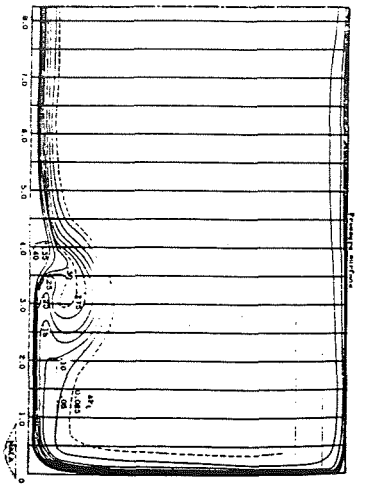

experiments

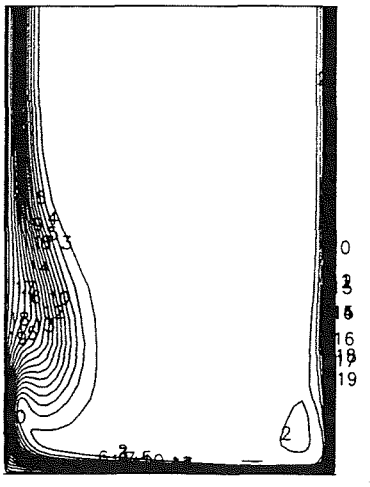

computations (51×41×31)

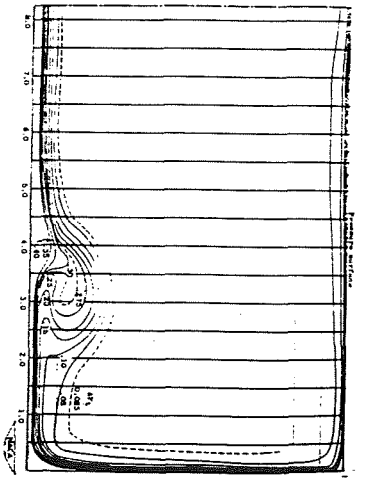

experiments

Figure 22. Stanitz elbow: Total pressure losses.